

Radiatively driven rotating pair-plasma jets from two component accretion flows

Indranil Chattopadhyay*

Centre for Plasma Astrophysics, Department of Mathematics, K. U. Leuven, Celestijnenlaan 200B, Leuven 3001, Belgium

Accepted . Received ; in original form

ABSTRACT

Centrifugal pressure of matter spiralling onto black holes, have long been known to produce standing or oscillating shocks. The post-shock disc puffs up in the form of a torus, which intercepts soft photons from the outer Keplerian disc and inverse Comptonizes them to produce hard photons. The post-shock region also produces jets. We study the interaction of both hard photons and soft photons, with rotating electron-positron jets. We show that hard photons from the post-shock torus are instrumental in acceleration of jets, while soft photons from the Keplerian disc is a better collimating agent. We also show that if the jets are launched closer to the black hole, relativistic and collimated jets are produced; if they are launched at larger distances both collimation and acceleration are less. We also show that if the shock location is relatively at larger distances from the black hole, collimation is better.

Key words: Accretion, accretion discs - black hole physics - radiation mechanism: general - radiative transfer - ISM: jets and outflows

1 INTRODUCTION

Jets in microquasars as well as in quasars shows relativistic terminal speed [*e.g.*, GRS 1915+105, Mirabel & Rodriguez (1994); 3C 273, 3C 345, Zensus *et al.* (1995); M87, Biretta (1993)], though the actual acceleration process is an enigma. It is well accepted in the scientific community that jets around compact objects originate from the accretion disc accompanying such compact objects. The study of interaction of radiation from the disc with

* E-mail: Indranil.Chattopadhyay@wis.kuleuven.ac.be

outflowing jets, is quite extensive. The radiation field produced by a disc, depends on the geometry as well as the dominant physical processes of the disc model. And hence the study of interaction of jets with radiation field produced by different disc models, will, in general, draw different conclusions.

Icke (1980) studied the effect of radiative acceleration of gas flow above a Keplerian disc, but did not consider the effect of radiation drag. Piran (1982), while calculating the radiative acceleration of outflows about the rotation axis of thick accretion discs, found out that in order to accelerate outflows to $\gamma > 1.5$ (where γ is the bulk Lorentz factor), the funnels must be short and steep, but such funnels are found to be unstable. In a very important paper, Icke (1989) considered blobby jets about the axis of symmetry of thin discs (Shakura & Sunyaev 1973; Novikov & Thorne 1973, hereafter NT73) and he obtained the ‘magic speed’ of $v_m = 0.451c$ (c — the velocity of light), v_m being the upper limit of terminal speed. (Fukue 1996) extended this study for rotating flow above a thin disc and drew similar conclusions, although for rotating flow, away from axis of symmetry the terminal speed was found out to be a little less than the magic speed of Icke. It was shown that rotating winds above thin disc, generally spreads as the radiation force along the azimuthal direction (generated because of disc rotation) increases the angular momentum of the flow, and are difficult to accelerate because of the presence of radiation drag term in the vertical direction (Tajima & Fukue 1996, 1998). Radiatively driven winds were also studied for radiation coming from a slim disc (Watarai & Fukue 1999). In spite of different disc temperature profile from the thin disc, and also the inclusion of advection term, radiatively driven outflows from slim disc concluded, that these radiation fields will spread the outflows and will suppress the vertical motion. Later Fukue and his collaborators, achieved relativistic terminal speed and collimation for pair-plasma jets from a disc model which contains inner ADAF region (non-luminous) and outer slim disc (luminous), for non-rotating black hole (Fukue *et al.* 2001), and repeated the same scheme for rotating black holes (Orihara & Fukue 2003). We are working in a different regime. We consider the TCAF (Two Component Accretion Flow) disc model (see, Chakrabarti & Titarchuk 1995, hereafter CT95), which consists of less luminous outer Keplerian disc and more luminous post-shock torus in the hard spectral-state of the disc. Chattopadhyay & Chakrabarti (2000) calculated the radiative force on optically thin jets in and around the axis of symmetry for radiations coming from the post-shock torus. Chattopadhyay & Chakrabarti (2002a) investigated the issue of radiative acceleration of normal plasma jets, by radiations only from the post-shock torus of TCAF disc,

and concluded that normal-plasma jets are indeed accelerated to mildly relativistic terminal speed. Chattopadhyay & Chakrabarti (2002b) also reported that hard radiations from the post-shock torus do not impose *any* upper limit for terminal speed. Chattopadhyay *et al.* (2004, hereafter Paper-I), solved the equations of photo-hydrodynamics for on-axis pair dominated jets for radiations coming from the whole of TCAF disc model. Paper-I concluded that terminal speed $v \sim 0.9c$ is easily achieved if the shock-location in accretion $x_s \sim \text{few} \times 10r_g$ (r_g =Schwarzschild radius), and the luminosity of the post-shock torus ($\equiv L_C$) is $\sim \text{few} \times 10\%$ the Eddington luminosity. Paper-I also showed that the special geometry of the post-shock torus ensures that, its contribution to various radiative moments dominates over that due to Keplerian disc. Thus radiations from Keplerian disc (of luminosity L_K) has a very marginal effect on determining the terminal speed of jets. Having shown this, it is only natural to study how rotating jets behave in the presence of the radiation field of the disc. The azimuthal component of the radiative force generated by the disc rotation, will try to spin up the jet, while radiative drag force in the same direction will try to carry away the angular momentum from the jet. So it is particularly interesting to study which of these two phenomena wins.

In this paper we study the interaction of radiations from the whole of TCAF disc and rotating jets. We show that the radiation from the CENBOL (CENtrifugal pressure-dominated BOundary Layer; see Chakrabarti *et al.* 1996, CTKE96) is the chief accelerating agent, while radiation from Keplerian disc has greater degree of collimation property. Both collimation and acceleration are much higher when the jet materials are launched closer to the axis of symmetry. We show that, if radiative processes is the dominant accelerating agent then, we can get highly relativistic and collimated jets only in moderate hard states (*i.e.*, $L_C \sim L_K$) and not in extreme hard states ($L_C \gg L_K$).

In the next Section, we present a brief account of the TCAF disc model. In §3, we present the model assumptions and the equations of motion. We give an account of the streamline coordinates which we use to solve the governing equations. We also compute ten independent moments of radiation field from such an disc. In §4, we present our solutions and finally in §5, we draw our conclusions.

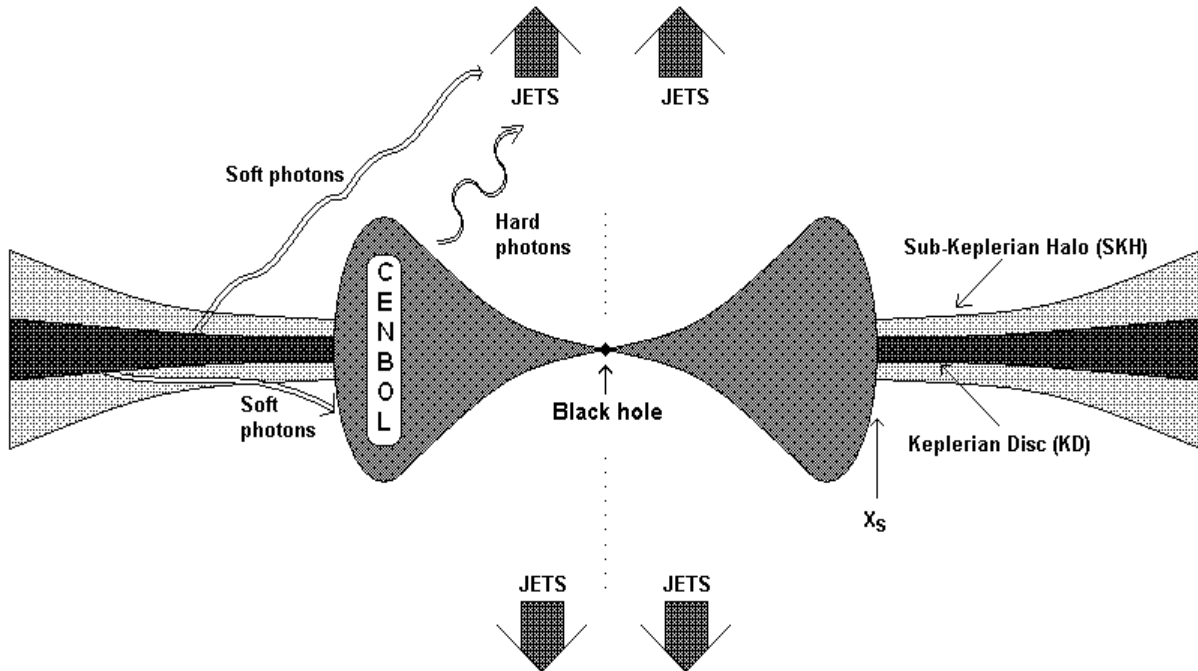


Figure 1. Cross-sectional view of Two Component Accretion Disc Model.

2 TCAF DISC

A detailed account of TCAF disc is given in Paper-I [also see, CT95; CTKE96; Chakrabarti 1997, hereafter C97, Chattopadhyay *et al.* (2003)]. For the sake of completeness, let us now give a brief account of the TCAF disc.

Inner boundary condition for matter accreting onto black holes are (i) supersonic and (ii) sub-Keplerian. Accretion topologies for sub-Keplerian matter admits two X-type critical points (Liang & Thompson 1980), and supersonic matter after crossing the outer critical point may undergo shock due to centrifugal pressure (Fukue 1987; Chakrabarti 1989, 1990, 1996). The post-shock matter then enters the black hole through the inner critical point. Matter is slowed down in the immediate post-shock region and as entropy is generated, it makes the post-shock region hot. This hot, slowed down post-shock region puffs up in the form of a torus the CENBOL.

Chakrabarti & Titarchuk (1995) for the first time proposed a disc model which contains both, Keplerian matter and sub-Keplerian matter. The Keplerian matter is of higher angular momentum and lower specific energy than the sub-Keplerian matter, and settles around the *equatorial plane* to form the *Keplerian disc* (hereafter KD). Sub-Keplerian matter flanks the cooler Keplerian disc from the top and bottom, sandwiching the Keplerian disc, and is known as the *sub-Keplerian halo* (hereafter SKH; also see, C97). The SKH suffers a shock at

a few tens of Schwarzschild radii. The shock compresses the post-shock flow making it denser than the pre-shock sub-Keplerian flow. The hot post-shock flow evaporates the Keplerian disc and falls to the black hole as a single component, in other words the shock location (x_s) is the outer boundary of CENBOL and the inner boundary of the KD. A schematic diagram of such a disc structure is shown in Fig. (1), where KD is shown to be sandwiched by SKH, and the position of x_s , as well as the central black hole are also shown. Although the SKH (pre-shock) is optically thin for the radiations from Keplerian disc, the post-shock torus is optically slim, in other words the optical depth of CENBOL is around unity (*i.e.*, $\tau \sim 1$; see CT95, CTKE96, C97 for details).

CT95 showed that, if the Keplerian accretion rate (\dot{M}_K) is higher than sub-Keplerian accretion rate (\dot{M}_h), then it supplies more soft photons to cool down the CENBOL. This results in more power to the soft end of the accretion disc spectrum — a state known as the *soft state*. If on the other hand, $\dot{M}_h > \dot{M}_K$, then SKH supplies more hot electrons to the CENBOL than the soft photons supplied by the KD. The dearth of soft photons cannot cool down the CENBOL significantly. Thus CENBOL remaining puffed up and hot, can intercept a significant fraction of soft photons produced by KD, and inverse-Comptonize them to produce the hard power-law tail of the accretion disc spectrum — a state called *hard state*. This kind of hybrid disc structure is known as the Two Component Accretion Flow or the TCAF disc (CT95; CTKE96; Ebisawa *et al.* 1996; C97), and has observational support (Smith *et al.* 2001, 2002).

Chakrabarti and his collaborators have also shown, the unbalanced thermal gradient force of CENBOL, in the z direction, drives a part of the in falling matter along the axis of symmetry to form jets (Chakrabarti 1998, 1999; Das & Chakrabarti 1999; Das *et al.* 2001). There are wide support that the jets are indeed coming out from a region within 50 – 100 Schwarzschild radius of the black hole (Junor *et al.* 1999). Similarly, it is believed that jets are produced only in hard states [see, Gallo *et al.* (2003), and references therein]. Thus it is natural to study interaction of hard radiation from the CENBOL and the outflowing jets, with the particular interest of studying, whether momentum deposited to the jet material by these hard photons can accelerate them to ultra-relativistic speeds.

It is to be remembered that, we are not considering generation mechanism of jets self-consistently. Since hard radiations are expected to emerge out of CENBOL, the hard photons ‘look’ directly into the jet vertically above and hence eventually deposit their momentum into the latter. Furthermore, radiation from a hot CENBOL is a likely source of pair production

and hence the possibility of radiative momentum deposition is likely to be higher even for radiations from CENBOL hitting the outflow at an angle [see, e.g., (Yamasaki *et al.* 1999) for production mechanism of pairs from hot accretion flows]. Thus we consider radiative momentum deposition on pair dominated jets, which are generated above the inner surface of CENBOL, *i.e.*, within the funnel like region.

3 ASSUMPTIONS, GOVERNING EQUATIONS AND COMPUTATION OF RADIATIVE MOMENTS FROM TCAF DISC

We ignore the curvature effects due to the presence of the central black hole mass. The metric is given by,

$$d\tilde{s}^2 = c^2 d\tilde{t}^2 - dr^2 - r^2 d\phi^2 - dz^2, \quad (1)$$

where, r , ϕ , and z are the usual coordinates in cylindrical geometry and $d\tilde{s}$ is the metric in four-space. The four-velocities are u^μ . The convention we follow is — the Greek indices signify all four components and the Latin indices represent only the spatial ones. The black hole is assumed to be non-rotating and hence the strong gravity is taken care of by the so-called Paczyński-Wiita potential (Paczyński & Wiita 1980).

In this paper, the generation mechanism of jets is not considered. We assume axis-symmetric, steady, rotating jets *i.e.*, $\partial/\partial\tilde{t} = \partial/\partial\phi = 0$. The derivation of the equations of motion of radiation hydrodynamics for optically thin plasma, was investigated by a number of workers. A detailed account of such derivation has been presented by Mihalas & Mihalas (1984) and Fukue (1996) [references therein], and are not presented here. The equations of motion are;

$$(\epsilon + p) \left(u^\mu \frac{\partial u^r}{\partial x^\mu} + \frac{GM_B r}{R(R - r_g)^2} - r u^\phi u^\phi \right) = -\frac{\partial p}{\partial r} - u^r u^\mu \frac{\partial p}{\partial x^\mu} + \rho \frac{\sigma_T}{mc} \mathfrak{S}^r, \quad (2a)$$

$$(\epsilon + p) \left(u^\mu \frac{\partial u^\phi}{\partial x^\mu} + \frac{2}{r} u^r u^\phi \right) = -u^\phi u^\mu \frac{\partial p}{\partial x^\mu} + \rho \frac{\sigma_T}{mcr} \mathfrak{S}^\phi, \quad (2b)$$

and

$$(\epsilon + p) \left(u^\mu \frac{\partial u^z}{\partial x^\mu} + \frac{GM_B z}{R(R - r_g)^2} \right) = -\frac{\partial p}{\partial z} - u^z u^\mu \frac{\partial p}{\partial x^\mu} + \rho \frac{\sigma_T}{mc} \mathfrak{S}^z. \quad (2c)$$

In above equations, ϵ , p and ρ are the internal energy, isotropic gas pressure and density measured in the co-moving frame of the fluid and $R = (r^2 + z^2)^{1/2}$. G , M_B , σ_T , m and $r_g(2GM_B/c^2)$ are the universal gravitational constant, the mass of the central black hole,

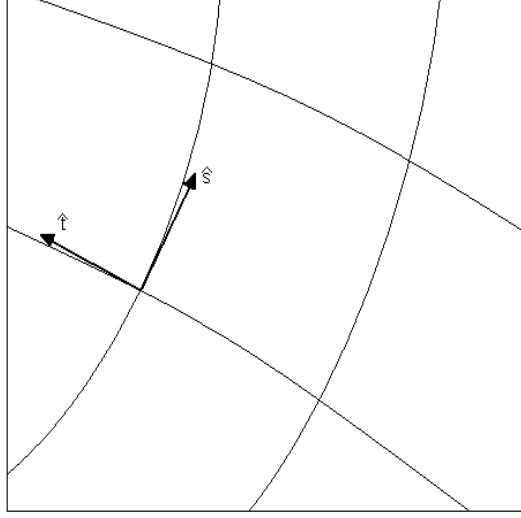


Figure 2. Schematic diagram of streamline coordinates (s, ϕ, t) in the meridional plane.

Thomson scattering cross-section, mass of the gas particles and Schwarzschild radius, respectively. \mathfrak{S}^i signifies radiative contributions along respective components of the momentum balance equation.

The radiative contributions are given by;

$$\begin{aligned} \frac{\sigma_T}{m} \frac{\mathfrak{S}^r}{c} &= \frac{\sigma_T}{m} \left[\gamma \frac{F^r}{c} - \gamma^2 u^r E - u^j P^{rj} + u^r \left(2 \frac{\gamma}{c} u^j F^j - u^j u^k P^{jk} \right) \right] \\ &= \left[\gamma f^r - \gamma^2 u^r \varepsilon - u^j \wp^{rj} + u^r \left(2\gamma u^j f^j - u^j u^k \wp^{jk} \right) \right] \end{aligned} \quad (3a)$$

Similarly,

$$\begin{aligned} \frac{\sigma_T}{m} \frac{\mathfrak{S}^\phi}{c} &= \frac{\sigma_T}{m} \left[\gamma \frac{F^\phi}{c} - \gamma^2 r u^\phi E - u^j P^{\phi j} + r u^\phi \left(2 \frac{\gamma}{c} u^j F^j - u^j u^k P^{jk} \right) \right] \\ &= \left[\gamma f^\phi - \gamma^2 r u^\phi \varepsilon - u^j \wp^{\phi j} + r u^\phi \left(2 \frac{\gamma}{c} u^j f^j - u^j u^k \wp^{jk} \right) \right] \end{aligned} \quad (3b)$$

and

$$\begin{aligned} \frac{\sigma_T}{m} \frac{\mathfrak{S}^z}{c} &= \frac{\sigma_T}{m} \left[\gamma \frac{F^z}{c} - \gamma^2 u^z E - u^j P^{zj} + u^z \left(2 \frac{\gamma}{c} u^j F^j - u^j u^k P^{jk} \right) \right] \\ &= \left[\gamma f^z - \gamma^2 u^z \varepsilon - u^j \wp^{zj} + u^z \left(2\gamma u^j f^j - u^j u^k \wp^{jk} \right) \right] \end{aligned} \quad (3c)$$

In Eqs. (3a-3c), $E(r, \phi, z)$, $F^i(r, \phi, z)$, and $P^{ij}(r, \phi, z)$ are the radiative energy density, three components of radiative flux and six components of radiative pressure tensors measured in observer frame, while $\varepsilon = \frac{\sigma_T}{m} E$, $f^i = \frac{\sigma_T}{mc} F^i$, and $\wp^{ij} = \frac{\sigma_T}{m} P^{ij}$. Furthermore, γ ($\gamma = u_t$) is the Lorentz factor. We assume the gas pressure to be negligible compared to the radiation pressure terms.

3.0.1 *Streamlines*

In streamline coordinates (s, ϕ, t) , s -axis (t -axis) is parallel (perpendicular) to streamlines, where $ds^2 = dr^2 + dz^2$, such that u^t is zero. In Fig. (2) we draw a schematic diagram of the streamline coordinates. The basic equations can then be written as (Fukue 1996; Fukue *et al.* 2001),

Momentum Balance along the streamline:

$$u^s \frac{\partial u^s}{\partial s} = -\frac{GM_B}{R(R-r_g)^2} \frac{rdr + zdz}{ds} + \frac{(r^2 u^\phi)^2}{r^3} \frac{dr}{ds} + \frac{\sigma_T}{cm} \tilde{\mathfrak{S}}^s, \quad (4a)$$

Angular Momentum conservation:

$$u^s \frac{\partial (r^2 u^\phi)}{\partial s} = \frac{\sigma_T}{cm} r \mathfrak{S}^\phi, \quad (4b)$$

And the streamline equation:

$$-\frac{GM_B}{R(R-2r_g)^2} \frac{rdz - zdr}{ds} + ru^\phi u^\phi \frac{dz}{ds} + (f^r \frac{dz}{ds} - f^z \frac{dr}{ds}) = 0, \quad (4c)$$

where,

$$\begin{aligned} \frac{\sigma_T}{m} \frac{\tilde{\mathfrak{S}}^s}{c} &= \gamma f^s - \gamma^2 \varepsilon u^s - (\wp^{ss} u^s + r \wp^{s\phi} u^\phi) + u^s \{2\gamma (f^s u^s + r f^\phi u^\phi) \\ &- (\wp^{ss} u^s u^s + 2r \wp^{s\phi} u^s u^\phi + r^2 \wp^{\phi\phi} u^\phi u^\phi)\}. \end{aligned} \quad (4d)$$

In Eq. (4d),

$$f^s = f^r \frac{dr}{ds} + f^z \frac{dz}{ds}$$

$$\wp^{ss} = \wp^{rr} \left(\frac{dr}{ds} \right)^2 + 2\wp^{rz} \frac{dz}{ds} \frac{dr}{ds} + \wp^{zz} \left(\frac{dz}{ds} \right)^2$$

and,

$$\wp^{s\phi} = \wp^{r\phi} \frac{dr}{ds} + \wp^{z\phi} \frac{dz}{ds}$$

Equations (4a-4c), can be simplified in terms of v and λ and can be expressed in geometric units ($r_g = c = M_B = 1$), for simplicity we will keep the same symbols representing various quantities defined so far.

We now define a three velocity measured by the static observer in geometrical units defined above,

$$v_s^2 = -\frac{u_s u^s}{u_{\tilde{t}} u^{\tilde{t}}}, \quad (5a)$$

while the angular-momentum and angular velocity are being defined as,

$$\lambda = -\frac{u_\phi}{u_{\tilde{t}}} \quad \& \quad \omega = \frac{u^\phi}{u^{\tilde{t}}}. \quad (5b)$$

We further define the 3-velocity measured by co-rotating observer,

$$v^2 = \frac{v_s^2}{1 - \omega\lambda}. \quad (5c)$$

So that $\gamma^2 = 1/(1 - v_s^2 - \omega\lambda) = 1/\{(1 - v^2)(1 - \omega\lambda)\} = \gamma_v^2\gamma_\lambda^2$, $u^s = \gamma_v v$, and $u^\phi = (\gamma\lambda)/r^2$.

Equations (4a-4c) are re-written as,

$$\frac{dv}{dz} = \frac{N_1}{D_1}, \quad (6a)$$

where,

$$\begin{aligned} N_1 = & [\gamma\mathcal{F}^s - \gamma^2\gamma_v v\mathcal{E} - \gamma_v v\mathcal{P}^{ss} - \gamma\frac{\lambda}{r}\mathcal{P}^{s\phi} + 2\gamma(\gamma_v^2 v^2\mathcal{F}^s + \gamma\gamma_v v\frac{\lambda}{r}\mathcal{F}^\phi) - \gamma_v^3 v^3\mathcal{P}^{ss} \\ & - 2\gamma\gamma_v^2 v^2\frac{\lambda}{r}\mathcal{P}^{s\phi} - \gamma^2\gamma_v v\frac{\lambda^2}{r^2}\mathcal{P}^{\phi\phi}] - \frac{1}{2R(R-1)^2} \left(r\frac{dr}{dz} + z \right) + \frac{(\gamma\lambda)^2}{r^3} \frac{dr}{dz}, \end{aligned} \quad (6b)$$

and

$$D_1 = \gamma^4 v. \quad (6c)$$

$$\frac{d\lambda}{dz} = \frac{N_2}{D_2} \quad (6d)$$

$$\begin{aligned} N_2 = & [\gamma\mathcal{F}^\phi - \gamma^3\frac{\lambda}{r}\mathcal{E} - \gamma_v v\mathcal{P}^{s\phi} - \gamma\frac{\lambda}{r}\mathcal{P}^{\phi\phi} + \gamma\frac{\lambda}{r}\{2\gamma(\gamma_v v\mathcal{F}^s + \gamma\frac{\lambda}{r}\mathcal{F}^\phi) - (\gamma_v^2 v^2\mathcal{P}^{ss} \\ & + 2\gamma\gamma_v v\frac{\lambda}{r}\mathcal{P}^{s\phi} + \gamma^2\frac{\lambda^2}{r^2}\mathcal{P}^{\phi\phi})\}]r - \gamma\gamma_v^3 v^2\lambda\frac{dv}{dz} + \gamma\gamma_v\gamma_\lambda^2 v\frac{\lambda^3}{r^3}\frac{dr}{dz} \end{aligned} \quad (6e)$$

$$D_2 = \gamma\gamma_v \left(1 + \frac{(\gamma\lambda)^2}{r^2} \right) v \quad (6f)$$

and,

$$\frac{dr}{dz} = \frac{-r/[2R(R-1)^2] + \gamma f^r + (\gamma\lambda)^2/r^3}{-z/[2R(R-1)^2] + \gamma f^z} \quad (6g)$$

Quantities defined in Eqs. (6b) and (6e) are:

$$\mathcal{F}^s = f^r \frac{dr}{dz} + f^z \quad (7a)$$

$$\mathcal{F}^\phi = f^\phi \frac{ds}{dz} \quad (7b)$$

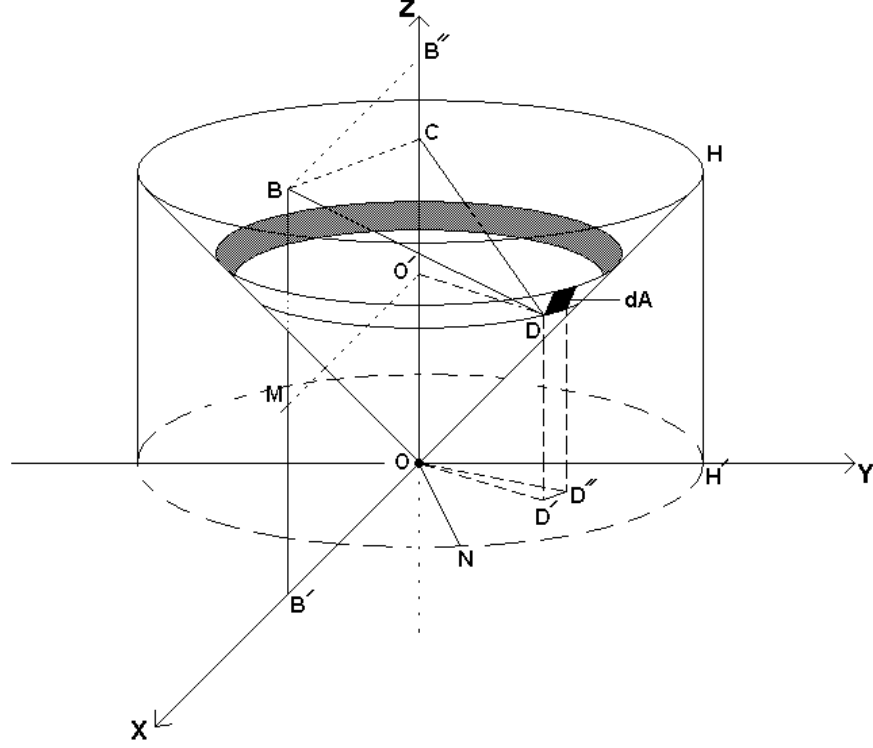


Figure 3. Cartoon diagram of CENBOL. The outer KD and SKH are not shown. $B(r, 0, z)$ is the field point and $D(x, \phi, y)$ is the source point on the inner surface of the CENBOL. The position of the black hole is at O . The inner surface of the CENBOL is assumed conical. The position of the black hole is O . $ON = x_s$, and $HH' = h_s$. $\angle B'OD' = \phi$ & $\angle D'OD'' = d\phi$. And dA is the differential area at D . Only the top half is shown.

$$\mathcal{E} = \varepsilon \frac{ds}{dz} \quad (7c)$$

$$\mathcal{P}^{ss} = \wp^{rr} \frac{dr}{dz} \frac{dr}{ds} + 2\wp^{rz} \frac{dr}{dz} + \wp^{zz} \frac{dz}{ds} \quad (7d)$$

$$\mathcal{P}^{s\phi} = \wp^{r\phi} \frac{dr}{dz} + \wp^{z\phi} \quad (7e)$$

$$\mathcal{P}^{\phi\phi} = \wp^{\phi\phi} \frac{ds}{dz}. \quad (7f)$$

We now have to solve Eqs. (6a), (6d) and (6g), for given radiation field $(\varepsilon, f^i, \wp^{ij})$, specified by disc parameters. It is to be noted that for motion along the axis $\lambda = 0$ and $\frac{dr}{dz} = \frac{d\lambda}{dz} = 0$, then Eq. (6a) reduces to Eq. (6) of Paper-I.

3.1 Computation of radiative moments from TCAF disc

The radiation reaching each point within the funnel like region and the region above it, is coming from two parts of the disc, namely, the CENBOL and Keplerian disc, hence all the radiative moments should have both the contributions.

In Fig. (3) a schematic diagram of the CENBOL is presented. The inner surface of the

CENBOL is assumed conical (described by, rotating OH about the axis of symmetry), and the outer surface of CENBOL is cylindrical (HH'). XOY describes the equatorial plane. O is the position of the black hole. $B(r, 0, z)$ is the field point where the various radiative moments are to be calculated. $D(x, \phi, y)$ is the source point on the CENBOL inner surface. $ON = OH' = x_s$ is the location of the shock. And $HH' = h_s$ is the shock height. The local normal at D is $\frac{DC}{|DC|}$. The differential area about D is marked as $d\mathcal{A}$. The shock height h_s depends on the shock location, and is expressed as $h_s \sim 0.6(x_s - 1)$ [see, Paper-I].

By definition, the radiative moments (in natural units) at B are;

$$E = \frac{1}{c} \int I d\Omega = \frac{1}{c} \left(\int_C I_C d\Omega_C + \int_K I_K d\Omega_K \right), \quad (8a)$$

$$\frac{F^i}{c} = \frac{1}{c} \int I l^i d\Omega = \frac{1}{c} \left(\int_C I_C l_C^i d\Omega_C + \int_K I_K l_K^i d\Omega_K \right), \quad (8b)$$

and

$$P^{ij} = \frac{1}{c} \int I l^i l^j d\Omega = \frac{1}{c} \left(\int_C I_C l_C^i l_C^j d\Omega_C + \int_K I_K l_K^i l_K^j d\Omega_K \right). \quad (8c)$$

In Eqs. (8a-8c), I , $d\Omega$, l^i are the frequency integrated intensity from the disc, differential solid angle at B , and the direction cosines at B w.r.t D , respectively. Suffix C and K represent quantities linked to CENBOL and the KD respectively. The expressions of solid angles subtended at B from D is given by

$$d\Omega_C = \frac{(d\mathcal{A}) \cos \angle CDB}{BD^2} = \frac{x \operatorname{cosec} \theta \, dx \, d\phi \, \cos \angle CDB}{BD^2}, \quad (8d)$$

where, $\cos \angle CDB = \frac{(BD^2 + CD^2 - BC^2)}{2(BD)(CD)}$, and $BD^2 = r^2 + x^2 + (z - y)^2 - 2 r x \cos \phi$, $CD = x \operatorname{sec} \theta$, $BC^2 = r^2 + (z - x \tan \theta - y)^2$ and $\theta [= \tan^{-1}(x_s/h_s)]$ is the semi-vertical angle of the CENBOL inner surface. Similarly it is easy to find from, Fig. (2), the direction cosines are given by, $l_C^r = (r - x \cos \phi)/BD$; $l_C^\phi = -(x \sin \phi)/BD$; and $l_C^z = (z - y)/BD$.

The frequency averaged CENBOL intensity is given by,

$$I_C = \frac{I_{C0}}{(1 + z_{\text{red}})^4} = \frac{L_C}{\pi \mathcal{A} (1 + z_{\text{red}})^4}, \quad (8e)$$

where, L_C and \mathcal{A} is the total CENBOL luminosity and total CENBOL area, z_{red} is the red-shift factor taken up to the first order of the disc velocity. The inner edge of CENBOL *i.e.*, also the TCAF disc is taken up to $x_{in} = 2r_g$, within which the general relativistic effect has to be considered. I_{C0} is assumed uniform for simplicity, as was explained in Paper-I.

We are not solving the disc-equations simultaneously, so we, in principle, cannot consider the Doppler shift of the photons coming out of CENBOL. Nonetheless, not considering the disc motion, robs us of a vital element of physics. The rotational velocity of the disc generates the ϕ component of the radiative flux. So we make an estimate of the post-shock

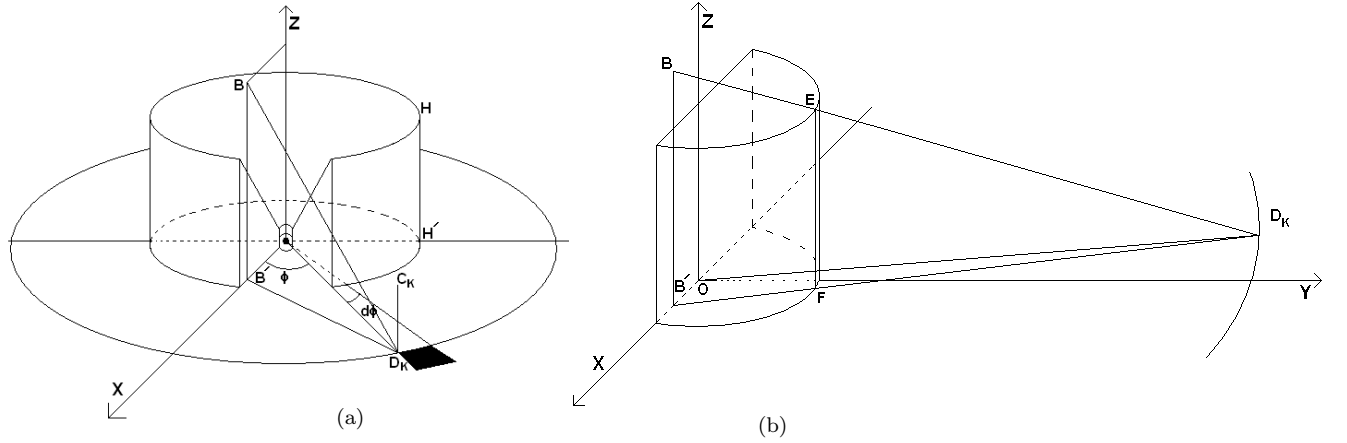


Figure 4. (a) Cartoon diagram of CENBOL. The outer Keplerian disc and sub-Keplerian halo are not shown. $B(r, 0, z)$ is the field point and $D(x, \phi, y)$ is the source point on the inner surface of the CENBOL. The inner surface of the CENBOL is assumed conical. The position of the black hole is also shown. $ON = x_s$, and $HH' = h_s$. $\angle B'OD' = \phi$ & $\angle D'OD'' = d\phi$. And dA is the differential area. (b) Cartoon diagram of CENBOL & Keplerian disc (KD) geometry. The SKH is not shown. $B(r, 0, z)$ is the field point and $D_K(x_K, \phi, 0)$ is the source point on the KD. The CENBOL is represented by the cylinder. The black spot represents O the position of the black hole. $OH' = x_s$, and $HH' = h_s$. And dA_K is the differential area at D_K (shaded).

disc motion. At the shock, the in-falling matter is virtually stopped. We solve the geodesic equation, starting from x_s with a very small velocity ($\approx 0.01c$). We assume the solution (\tilde{u}_{st}) [Appendix A] to be the 3-velocity of matter along the surface of the CENBOL. The angular momentum of the post shock matter is sub-Keplerian and almost constant [*e.g.*, CT95; Chakrabarti (1996)]; as the infall time-scale is much smaller than the viscous time-scale. So it is assumed to be constant, and is also the initial specific angular momentum ($\lambda_{in} = 1.7$ in the geometrical units defined above) of the jet. Under such assumptions, the radial, azimuthal and axial 3-velocity of the matter on the CENBOL surface is given by (expressed in dimensionless units described above), $\tilde{u}_x = \tilde{u}_{st} \sin\theta$, $\tilde{u}_\phi = (1 - 1/x)^{1/2} (\lambda_{in}/x)$ and $\tilde{u}_y = u_{st} \cos\theta$. Therefore $(1 + z_{red}) = (1 - \tilde{u}_i l^i)$, where

$$\tilde{u}_i l^i = \frac{(\tilde{u}_x \cos\phi - \tilde{u}_\phi \sin\phi)(r - x \cos\phi)}{BD} - \frac{(\tilde{u}_x \sin\phi + \tilde{u}_\phi \cos\phi)(x \sin\phi)}{BD} + \frac{\tilde{u}_y(z - y)}{BD}. \quad (8f)$$

In Fig. (4a-b), we represent a cartoon diagram of CENBOL and Keplerian disc (KD). In Fig. (4a), $D_K(x_K, \phi, 0)$ is the source point on the KD, and as in previous figure, $B(r, 0, z)$ is field point where the various moment are computed. In Fig. (4b), only one half of the CENBOL/KD geometry above the equatorial plane is shown. B is still the field point, but $D_K(x_K, \phi_f, 0)$ is the limit, up to which B can see the annulus on KD defined by radius (x_K), in the positive ϕ direction. So ϕ_f is the limit of integration for ϕ . From Fig. (4a), one can

easily find out,

$$d\Omega_K = \frac{dA_K}{BD_K^2} \cos \angle CDB = \frac{z x_K d\phi dx_K}{BD_K^3}, \quad (8g)$$

where, $BD_K^2 = r^2 + z^2 + x_K^2 - 2r x_K \cos\phi$, and the direction cosines are given by, $l_K^r = (r - x_K \cos\phi)/BD_K$; $l_K^\phi = -(x_K \sin\phi)/BD_K$; and $l_K^z = z/BD_K$.

The frequency averaged KD intensity (see, NT73) is given by,

$$I_K = \frac{I_{K0}}{(1 + \xi_{red})^4} = \frac{(3GM_B \dot{M}_K)/(8\pi^2 r_g^3) (x_K^{-3} - \sqrt{3}x_K^{-7/2})}{(1 + \xi_{red})^4}, \quad (8h)$$

Now, the Doppler shift term is given by $1 + \xi_{red} = 1 - \varpi_i l_K^i$, where,

$$\varpi_i l_K^i = -\tilde{u}_K \sin\phi \frac{r - x_K \cos\phi}{BD_K} - \tilde{u}_K \cos\phi \frac{x_K \sin\phi}{BD_K}. \quad (8i)$$

In the above equation $\tilde{u}_K = \sqrt{1/\{2(x_K - 1)\}}$ — the Keplerian velocity around a non-rotating black hole (in geometrical units).

Shadow effect of CENBOL on the jets:

As the jets are produced within the funnel like region of the TCAF disc, up to certain z the radiation from KD to the jet material, is blocked by the presence of CENBOL. It is easy to find from Figs. (3-4), that for material at a particular r ($< x_s$, as jets are produced from the CENBOL region), the radiations from KD is completely blocked for $z \leq h_s(x_o - r)/(x_o - x_s)$. But even for $z > h_s(x_o - r)/(x_o - x_s)$, the jet cannot ‘see’ the entire Keplerian disc. From Fig. (4b), it is clear that the jet material at B cannot see, the whole of the annular area defined by radius x_K , as part of it is blocked by the CENBOL. If for a particular r , $h_s(x_o - r)/(x_o - x_s) \leq z \leq h_s(x_K + r)/(x_K - x_s)$, then, from Fig. (4b), one can find an expression for ϕ_f ,

$$\phi_f = \cos^{-1} \left(\frac{x_K^2 + x_s^2 - FD_K^2}{2x_K x_s} \right) + \cos^{-1} \left(\frac{r^2 + x_s^2 - (B'D_K - FD_K)^2}{2rx_s} \right), \quad (8j)$$

where, $B'D_K^2 = r^2 + x_K^2 - 2rx_K \cos\phi_f$, and $FD_K = (h_s B'D)/r$. ϕ_f is to be computed numerically from Eq. (8j). For, $z > h_s(x_K + r)/(x_K - x_s)$, $\phi_f = 2\pi$. Eqs. (8a-8c) are integrated, with the help of Eqs. (8d-8j), to get the expressions of various radiative moments of a TCAF disc.

Let us now multiply, σ_T/m , with Eqs. (8a-8c), to get,

$$\begin{aligned} \varepsilon &= \varepsilon_{K0} \int_{x_s}^{x_o} \left[\int_0^{\phi_f} \frac{z(x_K^{-2} - \sqrt{3}x_K^{-5/2})d\phi'}{(r^2 + z^2 + x_K^2 - 2rx_K \cos\phi')^{3/2} (1 + \xi_{red})^4} \right. \\ &\quad \left. + \int_{\phi_f}^{2\pi} \frac{z(x_K^{-2} - \sqrt{3}x_K^{-5/2})d\phi'}{(r^2 + z^2 + x_K^2 - 2rx_K \cos\phi')^{3/2} (1 + \xi_{red})^4} \right] dx_K \end{aligned}$$

$$\begin{aligned}
& + \varepsilon_{C0} \int_{x_{in}}^{x_s} \int_0^{2\pi} \frac{(x^2 + y^2)^{1/2} \cos \angle CDB d\phi' dx}{(r^2 + z^2 + x^2 - 2rx \cos \phi')^{3/2} (1 + z_{red})^4} \\
& = \varepsilon_{K0} \tilde{E}_K(r, z, x_s, x_o) + \varepsilon_{C0} \tilde{E}_C(r, z, x_s, x_o) \\
& = \varepsilon_K + \varepsilon_C
\end{aligned} \tag{9a}$$

$$\begin{aligned}
f^i & = f_{K0} \int_{x_s}^{x_o} \left[\int_0^{\phi_f} \frac{z(x_K^{-2} - \sqrt{3}x_K^{-5/2}) l_K^i d\phi'}{(r^2 + z^2 + x_K^2 - 2rx_K \cos \phi')^{3/2} (1 + \xi_{red})^4} \right. \\
& + \left. \int_{\phi_f}^{2\pi} \frac{z(x_K^{-2} - \sqrt{3}x_K^{-5/2}) l_K^i d\phi'}{(r^2 + z^2 + x_K^2 - 2rx_K \cos \phi')^{3/2} (1 + \xi_{red})^4} \right] dx_K \\
& + f_{C0} \int_{x_{in}}^{x_s} \int_0^{2\pi} \frac{(x^2 + y^2)^{1/2} \cos \angle CDB l^i d\phi' dx}{(r^2 + z^2 + x^2 - 2rx \cos \phi')^{3/2} (1 + z_{red})^4} \\
& = f_{K0} \tilde{F}_K^i(r, z, x_s, x_o) + f_{C0} \tilde{F}_C^i(r, z, x_s, x_o) \\
& = f_K^i + f_C^i
\end{aligned} \tag{9b}$$

$$\begin{aligned}
\wp^{ij} & = \wp_{K0} \int_{x_s}^{x_o} \left[\int_0^{\phi_f} \frac{z(x_K^{-2} - \sqrt{3}x_K^{-5/2}) l_K^i l_K^j d\phi'}{(r^2 + z^2 + x_K^2 - 2rx_K \cos \phi')^{3/2} (1 + \xi_{red})^4} \right. \\
& + \left. \int_{\phi_f}^{2\pi} \frac{z(x_K^{-2} - \sqrt{3}x_K^{-5/2}) l_K^i l_K^j d\phi'}{(r^2 + z^2 + x_K^2 - 2rx_K \cos \phi')^{3/2} (1 + \xi_{red})^4} \right] dx_K \\
& + \wp_{C0} \int_{x_{in}}^{x_s} \int_0^{2\pi} \frac{(x^2 + y^2)^{1/2} \cos \angle CDB l^i l^j d\phi' dx}{(r^2 + z^2 + x^2 - 2rx \cos \phi')^{3/2} (1 + z_{red})^4} \\
& = \wp_{K0} \tilde{P}_K^{ij}(r, z, x_s, x_o) + \wp_{C0} \tilde{P}_C^{ij}(r, z, x_s, x_o) \\
& = \wp_K^{ij} + \wp_C^{ij}
\end{aligned} \tag{9c}$$

In Eqs. (9a-9c), the space-dependent part of ε , f^i , and \wp^{ij} are expressed as \tilde{E} , \tilde{F}^i and \tilde{P}^{ij} . Suffix ‘K’ and ‘C’ signify Keplerian and CENBOL contributions. If the moments are expressed in dimensionless units then the constants in Eqs. (9a-9c), are given by,

$$\varepsilon_{C0} = f_{C0} = \wp_{C0} = \frac{1.3 \times 10^{38} \ell_c \sigma_T}{2\pi c m \mathcal{A} G M_\odot} \tag{9d}$$

and

$$\varepsilon_{K0} = f_{K0} = \wp_{K0} = \frac{4.32 \times 10^{17} \dot{m}_k \sigma_{TC}}{32\pi^2 m G M_\odot}, \tag{9e}$$

where, $\ell_c = L_C/L_{\text{Edd}}$ (L_C — CENBOL luminosity & L_{Edd} — Eddington luminosity), $\dot{m}_k = \dot{M}_K/\dot{M}_{\text{Edd}}$ (\dot{M}_K — Keplerian accretion rate, \dot{M}_{Edd} — Eddington Accretion rate), and \mathcal{A} is the CENBOL surface.

For simplicity, we will not compute the shock location x_s or the the CENBOL luminosity

(L_C) – instead, we will supply them as free parameters. They can be easily computed from accretion parameters (Chakrabarti 1989, 1990; CT95; Das *et al.* 2001; Chattopadhyay *et al.* 2003).

To obtain all the components of radiation field, we supply the following disc-parameters, (a) the inner radius of the CENBOL $x_{in}(= 2r_g$, as explained in §3.1), (b) the shock location x_s , (c) the CENBOL luminosity ℓ_c (in units of L_{Edd}), (d) the Keplerian accretion rate \dot{m}_k .

The expression of Keplerian luminosity was given in Paper-I, and is;

$$L_K = r_g^2 \int_{x_s}^{x_o} 2\pi I_{K0} 2\pi x_K dx_K = \frac{3}{4} \dot{m}_k \left[-\frac{1}{x_K} + \frac{2}{3x_K} \sqrt{\frac{3}{x_K}} \right]_{x_s}^{x_o} L_{\text{Edd}} = \ell_k L_{\text{Edd}} \quad (10)$$

It is to be remembered, that as jets are only observed in intermediate to hard spectral states of the accretion disc, so we will constrain our analysis in the domain $\ell_k/\ell_c \sim 1$ to $\ell_k/\ell_c < 1$.

3.2 The components of radiation field

In Fig. (5), we show the contour plots of the space-dependent part of various moments of radiation due to the CENBOL. The shock location is $x_s = 20r_g$. The space variation of various moments due to the CENBOL is strongest within the funnel like region of the disc, so we only plot them within and above the funnel like region. Further as the jets are likely to be produced in this region, so this is the region that matters for our purpose. Contour plots of various moments are $\tilde{E}_C(r, z)$ [Fig (5a); max. value: 50.55], $\tilde{F}_C^r(r, z)$ [Fig. (5b); max/min value: 1.7/-5.42], $\tilde{F}_C^\phi(r, z)$ [Fig. (5c); max. value: 28.94], $\tilde{F}_C^z(r, z)$ [Fig. (5d); max/min values: 5.2/-1.19], $\tilde{P}_C^{rr}(r, z)$ [Fig. (5e); max. value: 14.62], $\tilde{P}_C^{r\phi}(r, z)$ [Fig. (5f); max/min values: 0.98/-1.66], $\tilde{P}_C^{rz}(r, z)$ [Fig. (5g); max/min values: 0.67/-1.39], $\tilde{P}_C^{\phi\phi}(r, z)$ [Fig. (5h); max value: 29.8], $\tilde{P}_C^{\phi z}(r, z)$ [Fig. (5i); max value: 4.4] and $\tilde{P}_C^{zz}(r, z)$ [Fig. (5j); max value: 3.88].

There are few features that are to be noted from the various moments of radiation, computed from the CENBOL:

- (i) The radiation field is highly anisotropic within the funnel like region of the CENBOL.
- (ii) All the moments maximize and have very sharp gradients around the inner edge x_{in} .
- (iii) Within the funnel (*i.e.*, for $r < x_s$ & $z \lesssim h_s$) $\tilde{F}_C^r < 0$, but at moderate values of r & z away from the black hole, $\tilde{F}_C^r > 0$.
- (iv) $\tilde{F}_C^z < 0$ very close to black hole.
- (v) $\tilde{F}_C^\phi > 0$ for $r > 0$ & $z > 0$.

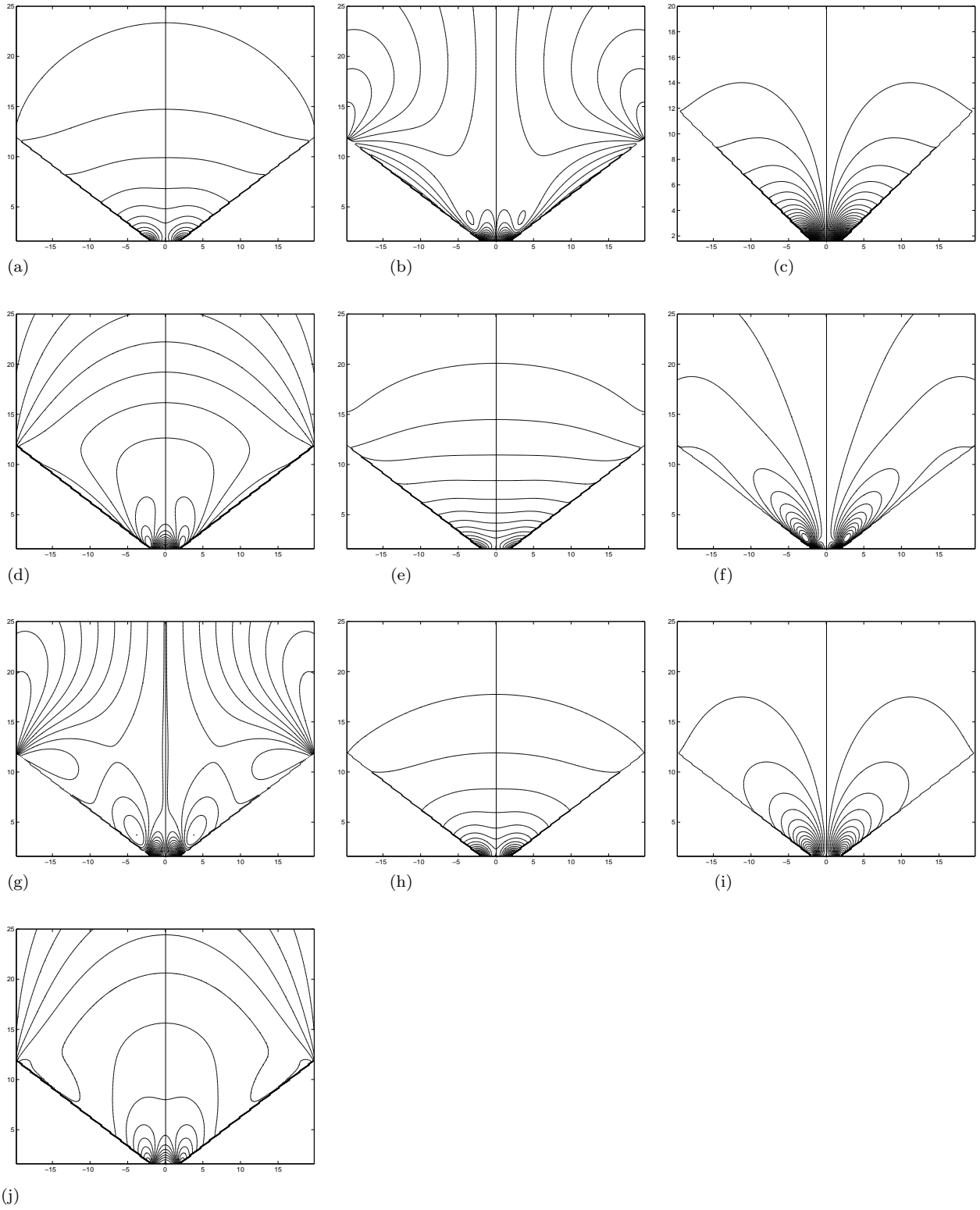


Figure 5. The space-dependent part of the ten independent components of radiation field due to the CENBOL. (a) $\tilde{E}_C(r, z)$, (b) $\tilde{F}_C^r(r, z)$, (c) $\tilde{F}_C^\phi(r, z)$, (d) $\tilde{F}_C^z(r, z)$, (e) $\tilde{P}_C^{rr}(r, z)$, (f) $\tilde{P}_C^{r\phi}(r, z)$, (g) $\tilde{P}_C^{rz}(r, z)$, (h) $\tilde{P}_C^{\phi\phi}(r, z)$, (i) $\tilde{P}_C^{\phi z}(r, z)$, (j) $\tilde{P}_C^{zz}(r, z)$. The disc parameters are $x_s = 20r_g$ & $x_{in} = 2r_g$.

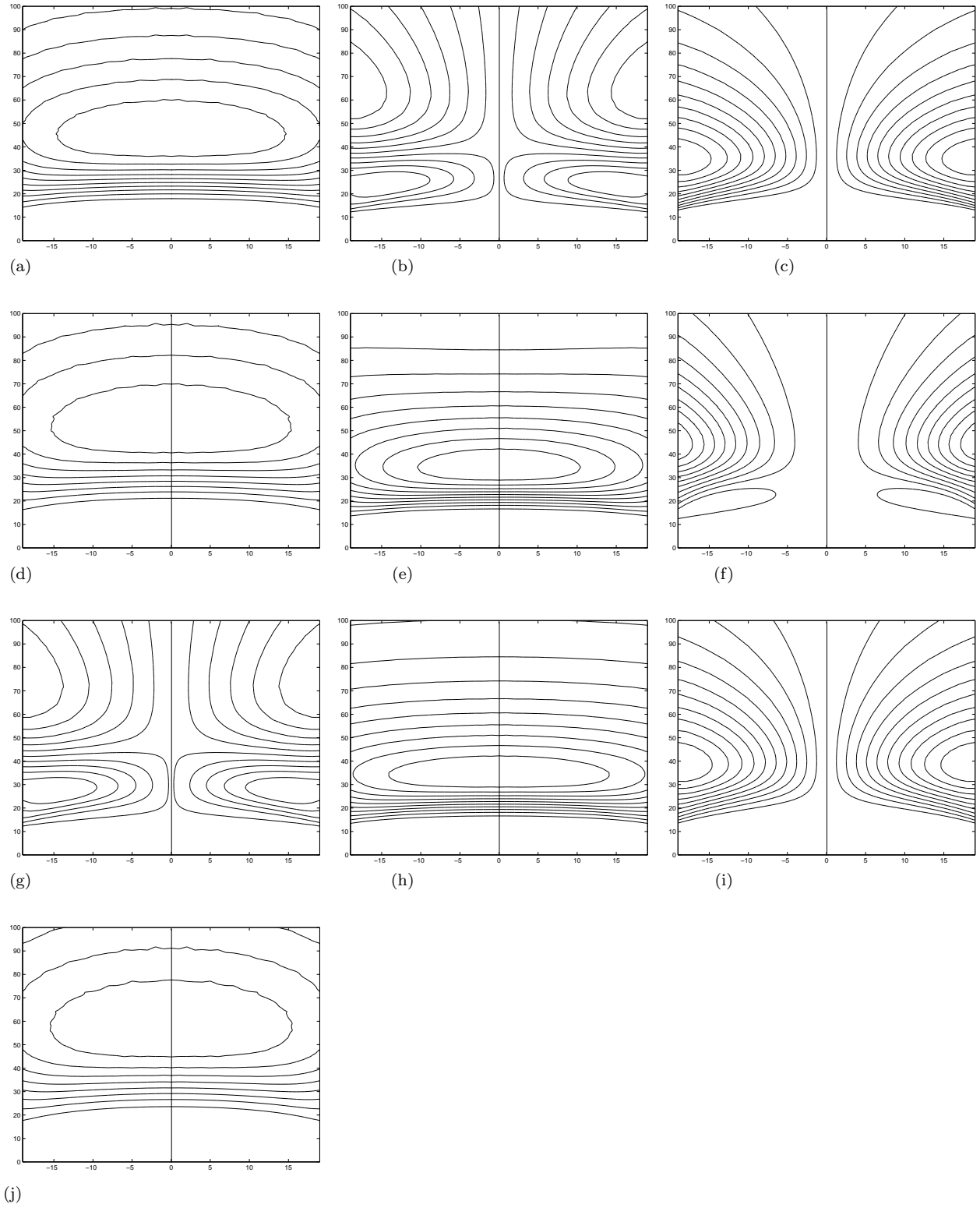


Figure 6. The space-dependent part of the ten independent components of radiation field due to the CENBOL. (a) $\tilde{E}_K(r, z)$, (b) $\tilde{F}_K^r(r, z)$, (c) $\tilde{F}_K^\phi(r, z)$, (d) $\tilde{F}_K^z(r, z)$, (e) $\tilde{P}_K^{rr}(r, z)$, (f) $\tilde{P}_K^{r\phi}(r, z)$, (g) $\tilde{P}_K^{rz}(r, z)$, (h) $\tilde{P}_K^{\phi\phi}(r, z)$, (i) $\tilde{P}_K^{\phi z}(r, z)$, (j) $\tilde{P}_K^{zz}(r, z)$. The disc parameters are $x_s = 20r_g$ & $x_o = 500r_g$.

(vi) At $r = 0$, $\tilde{F}_C^\phi = \tilde{F}_C^r = 0$.

(vii) At $r \sim x_{in}$ & $z \rightarrow \text{small}$, $\tilde{F}_C^\phi > \tilde{F}_C^z > \tilde{F}_C^r$.

(viii) At $r \sim x_{in}$ & $z \rightarrow \text{large}$, $\tilde{F}_C^\phi \approx \tilde{F}_C^r$ but less than \tilde{F}_C^z .

(ix) \tilde{E}_C is the most dominant of all the moments.

(x) $P_C^{rr} \lesssim P_C^{\phi\phi}$ & $P_C^{rr}(P_C^{\phi\phi}) > P_C^{zz}$.

(xi) $P_C^{r\phi} \approx P_C^{rz}$.

(xii) For $x_s \sim 10\text{--}20r_g$ & $R \rightarrow 100r_g$, the radiation field due to CENBOL approaches that due to a point source (Paper-I).

It is evident that, as z becomes small, $\tilde{F}_C^\phi > \tilde{F}_C^z > \tilde{F}_C^r$, still higher values of \tilde{E}_C & $\tilde{P}_C^{\phi j}$ will ensure that the λ gained by \tilde{F}_C^ϕ will be less than that reduced by the drag terms of Eq. (6d). It is also evident that as \tilde{F}_C^r changes from < 0 to > 0 , as one goes away from the black hole and the axis of symmetry, which means closer to the axis and the black hole, radiation from CENBOL would push the jet material towards the axis and further away it will tend to spread the jet. This doesnot mean that, more luminous the CENBOL, more is the spreading, since radiation drag along r -direction will limit the radial expansion of jet.

In Fig. (6), the contour maps of various moments of the radiation field due to the outer Keplerian disc is plotted. The shock location is same as Fig. (5). In contrast to the contribution due to the CENBOL, the Keplerian contribution is zero within the domain $r \leq x_s$, $z \leq h_s(x_o - r)/(x_o - x_s)$. The anisotropic nature of the radiation field extends to a region at much larger distances above the funnel like region of the CENBOL. The contour map of various moments from the Keplerian disc are, $\tilde{E}_K(r, z)$ [Fig. (6a); max. value: 2.23×10^{-5}], $\tilde{F}_K^r(r, z)$ [Fig. (6b); max/min values: $1.77 \times 10^{-6} / -1.12 \times 10^{-6}$], $\tilde{F}_K^\phi(r, z)$ [Fig. (6c); max. value: 8.62×10^{-7}], $\tilde{F}_K^z(r, z)$ [Fig. (6d); max. value: 1.7×10^{-5}], $\tilde{P}_K^{rr}(r, z)$ [Fig. (6e); max. value: 5.75×10^{-6}], $\tilde{P}_K^{r\phi}(r, z)$ [Fig. (6f); max/min values: $9.49 \times 10^{-8} / -1.37 \times 10^{-8}$], $\tilde{P}_K^{rz}(r, z)$ [Fig. (6g); max/min values: $1.25 \times 10^{-6} / -8.6 \times 10^{-7}$], $\tilde{P}_K^{\phi\phi}(r, z)$ [Fig. (6h); max. value: 5.75×10^{-6}], $\tilde{P}_K^{\phi z}(r, z)$ [Fig. (6i); max value: 5.9×10^{-7}] and $\tilde{P}_K^{zz}(r, z)$ [Fig. (6j); max. value: 1.4×10^{-5}].

As in the previous figure, there are few features to be noted in Fig. (6) too. They are:

(i) Each of the moments of the radiation field due to the KD is few orders of magnitude less than the corresponding ones due to CENBOL.

(ii) $\text{Max}(\tilde{F}_K^z) > \text{max}(\tilde{F}_K^r) > \text{max}(\tilde{F}_K^\phi)$. That means spreading of jets will be less.

(iii) The gradients of moments from the KD are lesser compared to that from the CENBOL.

(iv) $\tilde{F}_K^z > 0$.

(v) $\tilde{F}_K^r < 0$ in a larger domain \Rightarrow pushing the jet materials towards axis in a larger domain above the funnel of the CENBOL, and the angular momentum gained will also be less as (\tilde{F}_K^ϕ) is smallest of the three components of flux.

(vi) $\tilde{P}_K^{rr} \approx \tilde{P}_K^{\phi\phi} \approx \tilde{P}_K^{zz}$.

It is quite evident that in the hard state, Keplerian contribution to the radiative momentum will be marginal compared to the CENBOL contribution. But as \tilde{F}_C^r is weakest amongst all the components of CENBOL flux, and that \tilde{F}_K^r is directed towards the axis in a larger domain, thus for $\ell_k/\ell_c \lesssim 1$ it is possible to observe greater collimation.

It is to be noted in Figs. (5a-6j), that the various components of radiative moments computed in this paper are quantitatively different from earlier works on thin disc (Tajima & Fukue 1996, 1998), as well as, on slim disc (Watarai & Fukue 1999). When comparing radiation fields from thin disc and that from TCAF disc model, the first point to be noticed, is the geometry of the two disc model is different, secondly the disc motions are different, and thirdly the spatial variation of disc intensity (I_{CO} and I_{KO}) in TCAF model is different from that of purely thin disc. Even the radiative contribution from KD of the TCAF model to various radiative moments [Figs. (6a-6j)], differs from that computed by Tajima & Fukue (1998). The reasons are that (a) in Tajima & Fukue (1998), the inner radius of the thin disc is $3r_g$, while in this paper the inner radius of KD is x_s ($\sim \text{few} \times 10r_g$), so the jet does not ‘see’ the most luminous part of the KD, instead ‘sees’ the luminous CENBOL, and (b) the shadow effect of CENBOL. The shadow effect of CENBOL on jet material is extensively discussed in §3.1, we will just point out here that for jet material at $z \leq h_s(x_o - r)/(x_o - x_s)$, radiation from KD is completely blocked and for $z > h_s(x_o - r)/(x_o - x_s)$, the jet material only ‘sees’ a fraction of the outer rim of the KD. With increasing z , the jet ‘sees’ more and more inner part of the KD. In Tajima & Fukue (1998), such shadow effect was not considered and hence the difference in spatial variation of various radiative components between these two papers, namely between Figs. (6a-6j) of this paper and Figs. (2,3,4) of Tajima & Fukue (1998).

In Watarai & Fukue (1999), radiative moments are calculated for slim disc model, for three height to disc-radius ratio (H/R), (a) H/R \sim 0.05, (b) H/R \sim 0.4 and (c) H/R \sim 0.56. In the present paper, height to radius ratio of the CENBOL is $h_s/x_s \sim 0.57$ (for $x_s = 20r_g$, but is always < 0.6 for any higher x_s), so one might be tempted to think that, cases (b) and (c) of Watarai & Fukue (1999) should be similar to Figs. (5a-5j) of this paper. Components of

radiative moments are not solely determined by disc geometry, but also on the disc dynamics and its radiative properties, and the CENBOL and the slim disc models of Watarai & Fukue (1999) differ on both these counts. The radial velocity component of the slim disc considered was $v_r \sim c_1/r^{1/2}$ ($\equiv \tilde{u}_{st}$ in our case) and the azimuthal velocity to be $v_\phi \sim c_2/r^{1/2}$ ($\equiv \tilde{u}_\phi$, and c_1, c_2 depends on advection parameter, viscosity parameter, the ratio of specific heats, etc). The radial velocity of the CENBOL has no explicit analytical expression [computed in Appendix (A)], and, is not proportional to $r^{-1/2}$. In the immediate post-shock region, the radial velocity (\tilde{u}_{st}) of matter in CENBOL is much less than the radial velocity of matter in models (b) and (c) of Watarai & Fukue (1999), but close to the black hole it is higher. Even the nature of \tilde{u}_ϕ (in CENBOL) and v_ϕ (in slim disc) are different. The higher velocity components close to x_{in} , enhances the CENBOL intensity close to the black hole, and ultimately enhancing each of the radiative moments near the inner edge of the CENBOL compared to that achieved in slim disc.

This implies that the stream line velocity ($\sim 10^{-4}$) at the base of the jet above the CENBOL, will experience greater driving force but as the jet velocity is small there, the jet will experience less drag force. The opposite will be true for angular momentum: the drag forces will reduce angular momentum more than the jet may gain from the radiation, as λ_{in} is high at the jet base.

The other major difference in the two models is the difference in radiative property. The CENBOL radiation in the rest frame is uniform, while that of the slim disc model falls like r^{-2} . Thus the intensity at the outer edge of CENBOL is comparatively more significant than the slim disc case. This makes the radial flux directed inwards in a larger part of the domain above the CENBOL, compared to the region above the slim disc. In spite of the quantitative differences between the moments computed, by CENBOL and the slim disc, the overall qualitative similarity between Figs. (5a-5j) of this paper, and Figs. (4) of Watarai & Fukue (1999) is quite evident.

4 RESULTS

The results are obtained by integrating Eqs. (6a, 6d, 6g), in the radiation field of the TCAF disc given in Eqs (9a-9e). Apart from the disc-parameters supplied to calculate the radiation field from the disc, we also supply the injection radius of the jet r_i . As the jets are launched from the inner surface of the funnel like region of the CENBOL, the injection height (z_i)

should be just above the CENBOL inner surface. With no loss of generality we take $z_i = r_i(h_s/x_s) + 0.1$ in units of r_g . We assume that the outflow is made up of purely electron-positron pair plasma. We are interested to study the dependence of terminal speed as well as the relative spread of jets on disc parameters such as the ℓ_c , \dot{m}_k , x_s , r_{in} . We define r_∞/z_∞ as the relative spread of the jets, where r_∞, z_∞ are the cylindrical radial and axial coordinates at which $v \rightarrow v_\infty$. If $r_\infty/z_\infty < 0.1$, we define the jet as well collimated, $0.1 < r_\infty/z_\infty < 0.2$ as fairly collimated, $0.2 < r_\infty/z_\infty < 0.3$ as poorly collimated and so on.

4.1 Dependence on ℓ_c & \dot{m}_k :

In Fig. (7a), v_s is plotted with $\log(z)$, where the CENBOL luminosity is increased from $\ell_c = 0.2$ (long-dashed), $\ell_c = 0.3$ (dashed), $\ell_c = 0.4$ (solid) in units of L_{Edd} , while the Keplerian luminosity corresponds to $\dot{m}_k = 6$ (in units of \dot{M}_{Edd}) and $x_s = 20r_g$. The parameters which are kept constant through out the paper are, $v_{in} = 10^{-4}$, $\lambda_{in} = 1.7$, $x_{in} = 2r_g$ and $x_o = 500r_g$. The injection radius for the jet is $r_{in} = 3r_g$ in Figs. (7a-b). We see that the streamline velocity v_s increases with increasing ℓ_c , but the amount of increase in v_s for equivalent increase in ℓ_c , decreases.

This is to be expected as it was well documented in Paper-I, that CENBOL radiation is a good accelerator. Let us look at Fig. (7b), to see how the corresponding streamlines behave.

In Fig. (7b), the streamlines (z vs r) are plotted for $\ell_c = 0.2$ (long-dashed), $\ell_c = 0.3$ (dashed), $\ell_c = 0.4$ (solid), while $\dot{m}_k = 6$ is kept fixed. Other disc parameters are $x_s = 20r_g$ and $r_{in} = 3r_g$. As the CENBOL luminosity is increased, the streamlines are spreading. Though the spreading is decreasing for equivalent increase in ℓ_c , as in the case of streamline velocities. Before going into the reason for this let us probe into further details.

In Fig. (7c), terminal speed v_∞ is plotted with ℓ_c for $\dot{m}_k = 2$ (solid), $\dot{m}_k = 5$ (dashed) $\dot{m}_k = 8$ (long-dashed), other disc parameters being $r_{in} = 2r_g$ and $x_s = 20r_g$. Similar to Fig. (7a), we see that v_∞ increases appreciably with ℓ_c . For lower values of ℓ_c , v_∞ increases with \dot{m}_k , but decreases with increasing \dot{m}_k for higher values of ℓ_c . Although the change in v_∞ due to the change in \dot{m}_k is small compared to the change due to ℓ_c . This phenomenon was also reported in Paper-I. As this is rotating jet, we would naturally try to see how the jet λ behaves at large distances.

In Fig. (7d), λ_∞ is plotted with ℓ_c for $\dot{m}_k = 2$ (solid), $\dot{m}_k = 5$ (dashed) $\dot{m}_k = 8$

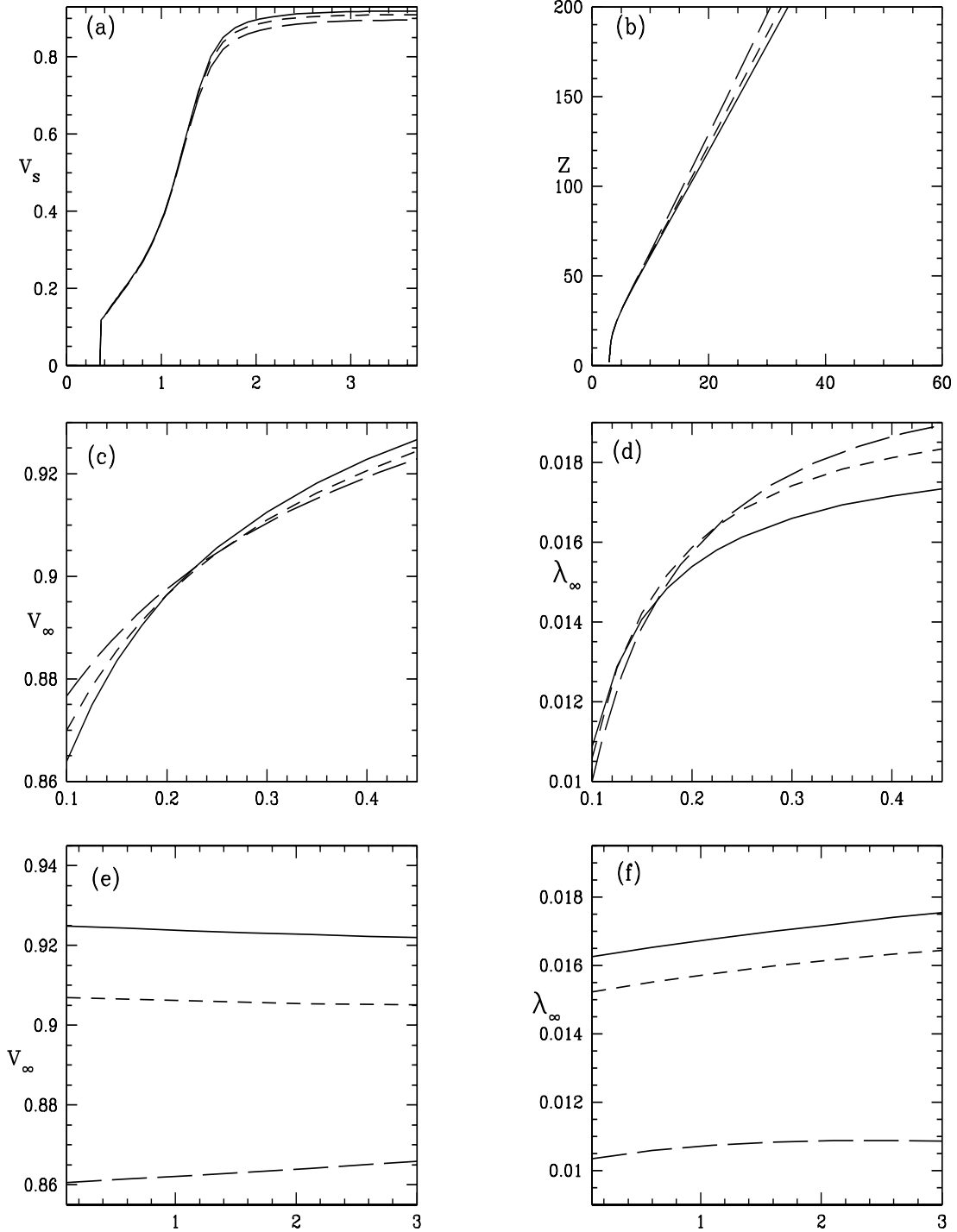


Figure 7. (a) Variation of v_s with $\log(z)$. Each of the curves represents $\ell_c = 0.2$ (long-dashed), $\ell_c = 0.3$ (dashed) and $\ell_c = 0.4$ (solid) in units of L_{Edd} . (b) The streamlines of the jet solution in the z - r plane, corresponding to $\ell_c = 0.2$ (long-dashed), $\ell_c = 0.3$ (dashed) and $\ell_c = 0.4$ (solid). For both the figures $\dot{m}_k = 6$, $r_{in} = 3r_g$. (c) Variation of terminal speed v_∞ with ℓ_c . Each curve represents $\dot{m}_k = 2$ (solid), $\dot{m}_k = 5$ (dashed), and $\dot{m}_k = 8$ (long-dashed), where $r_{in} = 2r_g$. (d) Variation of terminal specific angular momentum λ_∞ with ℓ_c . Each curve represents $\dot{m}_k = 2$ (solid), $\dot{m}_k = 5$ (dashed), and $\dot{m}_k = 8$ (long-dashed), where $r_{in} = 2r_g$. (e) Variation of terminal speed v_∞ with \dot{m}_k . Each curve represents $\ell_c = 0.1$ (long-dashed), $\ell_c = 0.25$ (dashed) and $\ell_c = 0.4$ (solid) in units of L_{Edd} . The injection radius of the jet is $r_{in} = 2r_g$. (f) Variation of terminal sp. angular momentum λ_∞ with \dot{m}_k . Each curve represents $\ell_c = 0.1$ (long-dashed), $\ell_c = 0.25$ (dashed) and $\ell_c = 0.4$ (solid) in units of L_{Edd} . The injection radius of the jet is $r_{in} = 2r_g$. For all the figures $v_{in} = 10^{-4}$, $\lambda_{in} = 1.7$, $x_{in} = 2r_g$, $x_s = 20r_g$ and $x_o = 500r_g$. Values of v_{in} , λ_{in} , x_{in} and x_o is kept constant through out the paper.

(long-dashed), other disc parameters being $r_{in} = 2r_g$ and $x_s = 20r_g$. We see that generally λ_∞ increases with ℓ_c . Within the funnel shape region of the CENBOL, the radiation field produces strong drag terms along ϕ direction which removes λ more than λ increased by f^ϕ , but further away from black hole λ reduces so much that the drag terms $[\propto \lambda(r, z)]$ become ineffective, and the jet gains angular momentum. So as the CENBOL becomes more and more luminous the jet gains angular momentum. Furthermore, for higher values of ℓ_c , λ_∞ increases with \dot{m}_k . This shows that KD radiation do not remove angular momentum any better than the CENBOL radiation.

In Fig. (7e), v_∞ is plotted with \dot{m}_k , parametrized by $\ell_c = 0.4$ (solid), $\ell_c = 0.25$ (dashed) and $\ell_c = 0.1$ (long-dashed). As was reported in Paper-I, v_∞ has a very weak dependence on \dot{m}_k . In Fig. (7f), λ_∞ is plotted with \dot{m}_k , parametrized by $\ell_c = 0.4$ (solid), $\ell_c = 0.25$ (dashed) and $\ell_c = 0.1$ (long-dashed). It is evident that λ_∞ has a very weak dependence on \dot{m}_k .

Let us now see the effect of radiation on spreading the jet. In Figs. (8a-b) we plot r_∞/z_∞ . In Fig. (8a), r_∞/z_∞ is plotted with ℓ_c , parametrized for $\dot{m}_k = 2$ (solid), $\dot{m}_k = 5$ (dashed) $\dot{m}_k = 8$ (long-dashed) [same parameters as Fig. (7c-d)], while in Fig. (8b), r_∞/z_∞ is plotted with \dot{m}_k , parametrized by $\ell_c = 0.4$ (solid), $\ell_c = 0.25$ (dashed) and 0.1 (long-dashed) [same parameters as Fig. (7e-f)]. The most remarkable contrast is that the jets are more collimated with increasing KD luminosity, while it tends to spread with increasing CENBOL luminosity. Though one must notice that spreading do not increase monotonically with ℓ_c , but tends to decrease with equivalent increase in ℓ_c . There are two features which are quite intriguing, (i) contrasting nature of CENBOL and KD radiation field in terms of collimation of the jet, and (ii) KD radiation seems to have nominal effect on determining v_∞ and λ_∞ , but plays relatively a greater role in collimation.

The reason that radiation from the KD can collimate the jets better than radiations from CENBOL, can be understood from Figs. (5-6) and Eq. (6g). We know that rotating matter tends to move away from the axis due to centrifugal force. If the angular momentum is reduced by the drag forces then the spreading may be arrested. Close to the CENBOL surface the radiation field is dominated by the CENBOL radiation and it produces large drag forces along ϕ . Further out as the jet starts to ‘see’ KD radiation, λ is reduced to the extent the drag force becomes marginal and the jet starts to gain some angular momentum. From Figs. (5-6), it is evident that the contributions from KD to the total radiation field is much less than that of the CENBOL so, angular momentum removed or added to the jet by the radiation from KD is marginal [*e.g.*, Fig. (7f)]. From Eq. (6g), it is clear that the

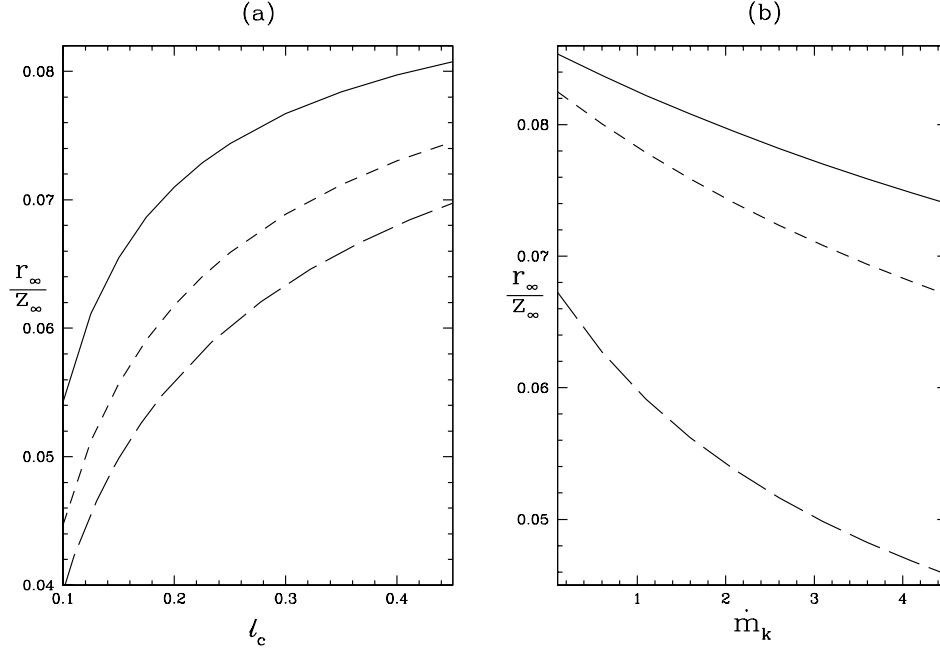


Figure 8. (a) Variation of r_∞/z_∞ with ℓ_c . Each curve represents $\dot{m}_k = 2$ (solid), $\dot{m}_k = 5$ (dashed). (b) Variation of r_∞/z_∞ with \dot{m}_k . Each curve represents $\ell_c = 0.4$ (solid), $\ell_c = 0.25$ (dashed) and $\ell_c = 0.1$ (long-dashed). The curves are drawn for $x_s = 20r_g$.

spreading of jets depends as much on centrifugal force, as on f^r . From the discussion below Figs. (5-6), we know that, \tilde{F}_C^r is weakest amongst all the \tilde{F}_C^i 's, while $\tilde{F}_K^r \lesssim \tilde{F}_K^z$ but $\tilde{F}_K^r > \tilde{F}_K^\phi$, and \tilde{F}_K^r is towards the axis in a larger domain. Thus when ℓ_c increases it doesnot help in collimation, but as \dot{m}_k increases the higher negative values of \tilde{F}_K^r , makes f^r more and more negative, and so it pushes the jet towards the axis of symmetry and helps in collimation, inspite of not removing angular momentum to the extent as CENBOL radiation does.

4.2 Dependence on r_i :

In Fig. 9, we show the effect of injection radius of the jets. In Fig. (9a), streamlines are plotted for $r_i = 2r_g$ (solid), $r_i = 3r_g$ (dashed), $r_i = 4r_g$ (long-dashed), $r_i = 5r_g$ (dashed-dotted), and $r_i = 6r_g$ (long dashed-dotted), where $\ell_c = 0.4$, $\dot{m}_k = 6$ and $x_s = 20r_g$. In Fig. (9b), corresponding λ distribution is shown along the streamlines for $r_i = 2r_g$ (solid), $r_i = 3r_g$ (dashed), $r_i = 4r_g$ (long-dashed), $r_i = 5r_g$ (dashed-dotted), and $r_i = 6r_g$ (long dashed-dotted), where $\ell_c = 0.4$, $\dot{m}_k = 6$ and $x_s = 20r_g$. From both the figures we see that the injection height z_i changes with r_i as has been discussed at the start of this section. It is evident that the as the injection radius is varied, the angular momentum of the jets are

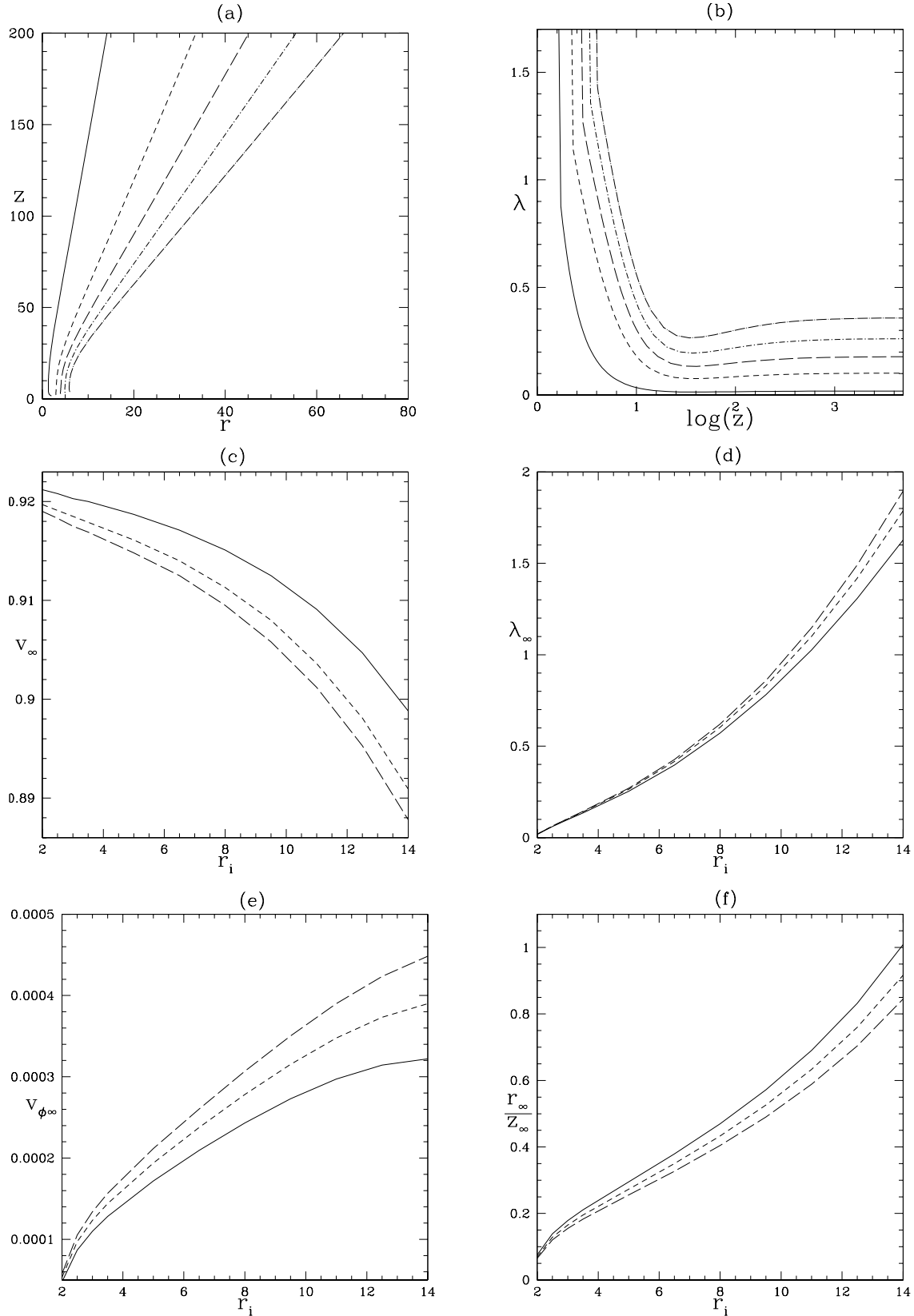


Figure 9. (a) Streamlines for $r_i = 2r_g$ (solid), $r_i = 3r_g$ (dashed), $r_i = 4r_g$ (long dashed), $r_i = 5r_g$ (dashed-dotted) & $r_i = 6r_g$ (long dashed-dotted); $\ell_c = 0.4$, $\dot{m}_k = 6$. (b) λ vs $\log(z)$, corresponding to the previous figure. (c) v_∞ vs r_i , (d) λ_∞ vs r_i , (e) $v_{\phi\infty}$ vs r_i , and (f) r_∞/z_∞ vs r_i ; for $\dot{m}_k = 4$ (solid), $\dot{m}_k = 7$ (dashed) & $\dot{m}_k = 10$ (long dashed). For all the figures $x_s = 20r_g$.

higher and it spreads further. The angular momentum of the jets at different r_i is same, but the radiative moments just above the CENBOL surface decreases with r . In other words the jets will gain less λ from the radiation field, but at the same time they will lose less λ due to the drag terms. The net effect is that with increasing r_i the jets are of higher angular momentum and thus these jets are less collimated.

On the other hand, jets are generated with very low velocity at the base ($\sim r_i$), so the drag term is negligible, but as all the radiative moments decreases with r above the CENBOL surface, the driving that the jets get due to f^r & f^z is much less as r_i is increased. In Figs. (9c-f), various terminal values are plotted with r_i , for $\dot{m}_k = 4$ (solid), $\dot{m}_k = 7$ (dashed) and $\dot{m}_k = 10$ (long-dashed), other parameters being $\ell_c = 0.4$, $x_s = 20r_g$. In Fig. (9c), we see that v_∞ decreases with r_i , but for fixed values of r_i , it increases with lower value of \dot{m}_k or in other words higher value of ℓ_c/ℓ_k . It has been observed in Paper-I and also in Fig. (7c) of this paper, that for $\ell_c \gtrsim 0.22$, v_∞ decreases with increasing \dot{m}_k . In Fig. (9d), on the other hand shows that λ_∞ increasing with increasing r_i . In Fig. (9e), the rotational velocity [$v_\phi^2 = -u_\phi u^\phi / u_t u^t$] at infinity ($v_{\phi\infty}$) is plotted with r_i . Similar to λ_∞ , $v_{\phi\infty}$ also increases with r_i . A interesting feature is seen if one compares Fig. (9f), with the previous two. In Fig. (9f), the relative spread r_∞/z_∞ is shown to increase with r_i , but the interesting feature is, as one increases \dot{m}_k , r_∞/z_∞ decreases, but both λ_∞ as well as $v_{\phi\infty}$ increases. This vindicates Eq. (6g), which says, f^r and f^z determines the streamlines along with the centrifugal force.

4.3 Dependence on x_s :

Until now we have investigated the solutions for $x_s = 20r_g$. We now concentrate on the dependence of jet solutions on x_s .

In Fig. (10a), v_∞ is plotted with x_s , for $\ell_c = 0.4$ (solid), $\ell_c = 0.25$ (dashed) and $\ell_c = 0.1$ (long-dashed), where $\dot{m}_k = 3$ and $r_i = 2r_g$ are kept fixed. With increasing values of x_s , the CENBOL intensity decreases and the driving force goes down, producing lesser terminal speed. We plot λ_∞ , corresponding to the cases in Fig. (10a), in Fig. (10b). Similar to v_∞ , λ_∞ also decreases with x_s . The reason for this is same as in the previous case, *i.e.*, the CENBOL intensity decreases with increasing x_s . Interestingly, as ℓ_c is increased, v_∞ increases appreciably but λ_∞ is increased marginally. Close to the injection radius, the λ of the jet decreases rapidly [see, Fig. (9b)], and then when at large distances from the disc, λ becomes too low so that the drag in the azimuthal direction becomes negligible, the jet starts to gain

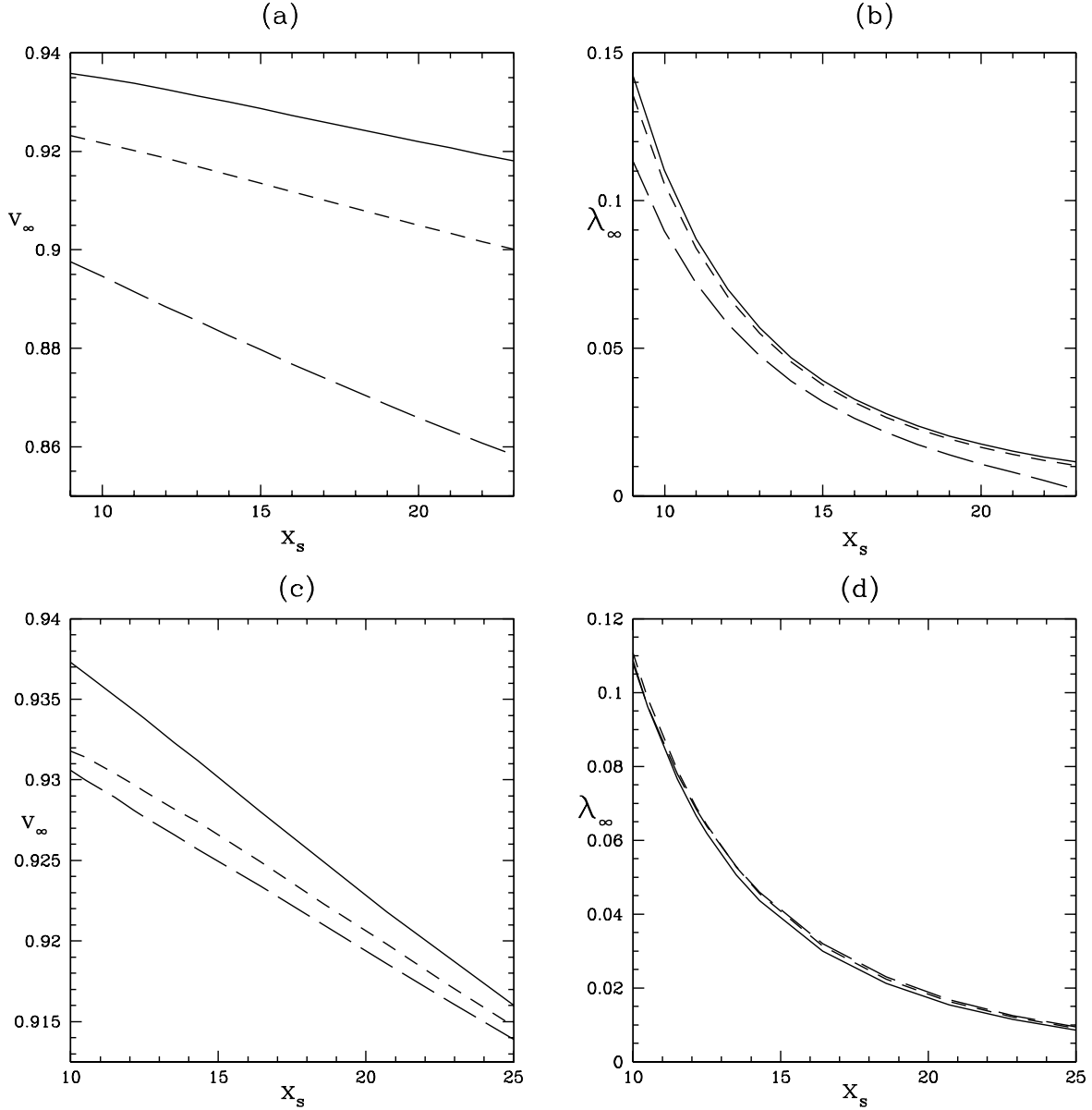


Figure 10. (a) Variation of v_∞ with x_s , $\ell_c = 0.4$ (solid), $\ell_c = 0.25$ (dashed), $\ell_c = 0.1$ (long-dashed), for constant $\dot{m}_k = 3$. (b) Variation of λ_∞ with x_s , $\ell_c = 0.4$ (solid), $\ell_c = 0.25$ (dashed), $\ell_c = 0.1$ (long-dashed), for constant $\dot{m}_k = 3$. (c) Variation of v_∞ with x_s , $\dot{m}_k = 2$ (solid), $\dot{m}_k = 5$ (dashed), $\dot{m}_k = 8$ (long-dashed) for $\ell_c = 0.4$. (d) Variation of λ_∞ with x_s . $\dot{m}_k = 2$ (solid), $\dot{m}_k = 5$ (dashed), $\dot{m}_k = 8$ (long-dashed) for $\ell_c = 0.4$. For all the figures $r_i = 2r_g$.

some angular momentum from the radiation. So increasing ℓ_c will produce higher λ_∞ , but as the gain in λ occurs at distances farther away from the disc, the radiative moments falls off anyway, so the increase in λ_∞ is small.

In Fig. (10c), v_∞ is plotted with x_s , for $\dot{m}_k = 2$ (solid), $\dot{m}_k = 5$ (dashed) and $\dot{m}_k = 8$ (long-dashed), with constant $\ell_c = 0.4$. The general conclusion that v_∞ decreases with increasing x_s is still valid, though increasing \dot{m}_k decreases v_∞ . Another difference we do notice is, the curve of v_∞ widens with increasing x_s , for higher values of ℓ_c in Fig. (10a), while in

Fig. (10c), v_∞ curves converges with increasing x_s . The reason is one and the same, *i.e.*, with increasing x_s , the KD contribution to all the components of radiative moments decreases and the CENBOL contribution dominates. As CENBOL radiation is a good accelerator, so for higher x_s , increasing ℓ_c produces higher v_∞ relative to the case where \dot{m}_k is increased.

In Fig. (10d), λ_∞ is plotted with x_s , for $\dot{m}_k = 2$ (solid), $\dot{m}_k = 5$ (dashed) and $\dot{m}_k = 8$ (long-dashed), with constant $\ell_c = 0.4$. λ_∞ decreases with x_s but has almost no dependence on KD radiation. This is because the azimuthal component of the radiative flux produced by KD is smaller compared to the other components (see §3.2).

In Fig. (11a), relative spread r_∞/z_∞ is plotted with x_s , for the same parameters as Fig. (10a-b), *i.e.*, for $\ell_c = 0.4$ (solid), $\ell_c = 0.25$ (dashed) and $\ell_c = 0.1$ (long-dashed), where $\dot{m}_k = 3$ and $r_i = 2r_g$ are kept fixed. We find r_∞/z_∞ decreases with increasing x_s . As λ_∞ decreases with increasing x_s [see, Fig. (10b)], so it is not surprising that there would be greater collimation. Still for fixed values of x_s , the difference in λ_∞ is marginal, while on the other hand the difference in r_∞/z_∞ is larger! If we turn our attention to Fig. (11b), which is plotted for $\dot{m}_k = 2$ (solid), $\dot{m}_k = 5$ (dashed) and $\dot{m}_k = 8$ (long-dashed), with constant $\ell_c = 0.4$ [same case as Fig. (10c-d)], it is again seen that, r_∞/z_∞ generally decreases with x_s , at the same time, decrement of r_∞/z_∞ for fixed values of x_s with increasing \dot{m}_k is larger, although λ_∞ is almost indistinguishable. From Figs. (10a-d), we know why v_∞ and λ_∞ decreases with increasing x_s . But increasing collimation is partly due to decreasing λ_∞ , otherwise variation of r_∞/z_∞ would have just mirrored the variation of λ_∞ . Increasing x_s makes f_C^r negative in a larger part of the funnel like region. Simultaneously, though radiative contributions by KD becomes weaker, none the less it makes $f_K^r < 0$ in a still larger part of the domain. Hence the combination of decreasing angular momentum as well as $f^r < 0$ in a larger region around the axis, collimates the jets to a greater degree.

Thus we conclude from Figs. (10a-d, 11a-b), if $\ell_c > 0.2$, $x_s > 20r_g$ then jets with terminal properties $v_\infty \gtrsim 0.9c$ and $r_\infty/z_\infty < 0.1$ is possible.

It will be interesting if these results are contrasted with earlier works. It is natural that these results would differ from earlier works, since the radiation field of TCAF disc is different from either thin (Tajima & Fukue 1998) or slim disc (Watarai & Fukue 1999). For both the disc models thin and slim, radiation field generally spreads the jet, and due to radiation drag the radiation field suppresses the motion along z direction. In another model (Fukue *et al.* 2001), where the authors considered inner non-luminous disc and outer luminous disc, the jets got collimated with increasing disc luminosity and the angular momentum

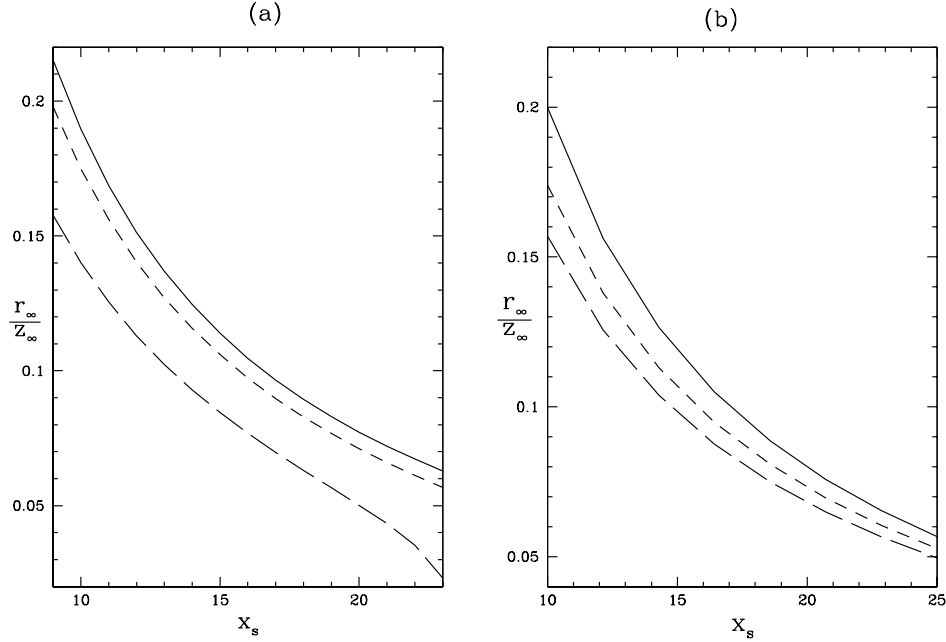


Figure 11. Variation of r_∞/z_∞ with x_s . (a) $\ell_c = 0.4$ (solid), $\ell_c = 0.25$ (dashed), $\ell_c = 0.1$ (long-dashed), for constant $\dot{m}_k = 3$. (b) $\dot{m}_k = 2$ (solid), $\dot{m}_k = 5$ (dashed), $\dot{m}_k = 8$ (long-dashed) for $\ell_c = 0.4$. Variation of λ_∞ with x_s . For all the figures $r_i = 2r_g$.

got decreased too. The reason for collimation is that the injection radius of the jet r_i (r_0 in their nomenclature) is less the inner boundary of the disc x_{in} (r_B in their nomenclature). This makes the radial flux $f^r < 0$ in a larger region above (and below) the disc surface, and it pushes the jet material towards the axis. Along with this, radiation drag reduces angular momentum, so the jets are collimated. In both the earlier papers Tajima & Fukue (1998) and Watarai & Fukue (1999), the injection radius is greater than the inner radius of the disc, which produces $f^r > 0$ which pushes the jets outwards, at the same time the maximum of f^ϕ is in and around the injection radius, which manages to spin up the jet further, these two effects combines to increase the angular momentum of the jets even more. *So the crucial point for collimation is whether or not $f^r < 0$.*

TCAF disc model has two radiation sources the CENBOL and the outer KD, and $r_i > x_{in}$. Jets from TCAF model starts with very low streamline velocity ($v_{in} = 10^{-4}$), and moderately high initial angular momentum ($\lambda_{in} = 1.7 \equiv$ angular momentum of the CENBOL). As the radiative energy density (ε) and the pressure components (\wp^{ij}) are quite intense close to the inner edge of the disc, the higher value of λ_{in} ensures very high drag force along ϕ . As a result, the jet λ is reduced appreciably, close to the injection radius [*e.g.*, Fig. (9b)]. Apart from reduction of the angular momentum of the jets, the radial flux f_r is negative, just above the CENBOL surface, and this collimates the jets. On the other hand,

as v_{in} is very small (i.e. drag along streamline is small), resulting in the jets being accelerated very fast, shooting upto $30 - 40r_g$ almost vertically, or sometimes initially pushed towards the axis [*e.g.*, Figs. (7b, 9a)]. At above $30 - 40r_g$ above the CENBOL surface $f_r > 0$, and the drag along ϕ is weakened [as, discussed in §4.1], these facts tend to spread the jet, although the spreading is arrested by KD luminosity, as well as, by the weakening of the f_C^ϕ .

One must also remember that, in jets around TCAF model, $r_i > x_{in}$. For $r_i \approx x_{in}$, radiations from the CENBOL region $x_{in} - r_i$ is negligible, and hence f^r is more negative near r_i , but for $r_i > x_{in}$, radiations from the CENBOL region $x_{in} - r_i$ cannot be neglected, making f^r is less negative near r_i . Thus we see for smaller values of r_i collimation and acceleration of jets are better [*e.g.*, Figs. (9a-9f)].

Although λ_∞ increases with ℓ_c , but one must notice that $\lambda_\infty \ll \lambda_{in}$ [*e.g.*, Figs. (7d, 10b, 10c)], which points to the fact, that indeed λ is reduced by drag force. One must also notice, that jets are more collimated by increasing outer KD luminosity [*e.g.*, Fig. (8b)], or increasing x_s [*e.g.*, Fig. (11b)], basically means that jets are basically collimated by $f^r < 0$, as was indicated by Fukue *et al.* (2001).

4.4 Dependence on ℓ_k/ℓ_c :

Until now in this section, we have seen that increasing ℓ_c produces faster jets, while increasing \dot{m}_k and x_s makes the jets more collimated. We have also seen that increasing r_i produces less v_∞ and the collimation is worse. The information of CENBOL radiation is provided by its luminosity, the information of KD radiation is supplied by \dot{m}_k and x_s , so to get a better understanding, we now study how the relative proportions of CENBOL and KD luminosity affect the jet solutions.

In Fig. (12a), v_∞ is plotted with ℓ_k/ℓ_c , for $\ell_c = 0.5$ (solid), $\ell_c = 0.3$ (dashed) and $\ell_c = 0.1$ (long-dashed), and $x_s = 20r_g$, $r_i = 2r_g$ are kept fixed. As in Fig. (7e), we find that the increasing ℓ_k from 10% to 100% of ℓ_c , has a marginal effect on v_∞ . In Fig. (12b), corresponding r_∞/z_∞ is plotted with ℓ_k/ℓ_c , *i.e.*, for $\ell_c = 0.5$ (solid), $\ell_c = 0.3$ (dashed) and $\ell_c = 0.1$ (long-dashed), and $x_s = 20r_g$, $r_i = 2r_g$ are kept fixed. Though v_∞ is marginally dependent on ℓ_k/ℓ_c , r_∞/z_∞ has a stronger dependence on ℓ_k/ℓ_c . In other words, KD radiations are not strong accelerators but definitely a better collimator. As has been discussed in §4.1, the radial flux due to KD is directed towards the axis in a larger domain, and as the ratio $\ell_k/\ell_c \gtrsim 0.5$ we find highly relativistic and collimated jets.

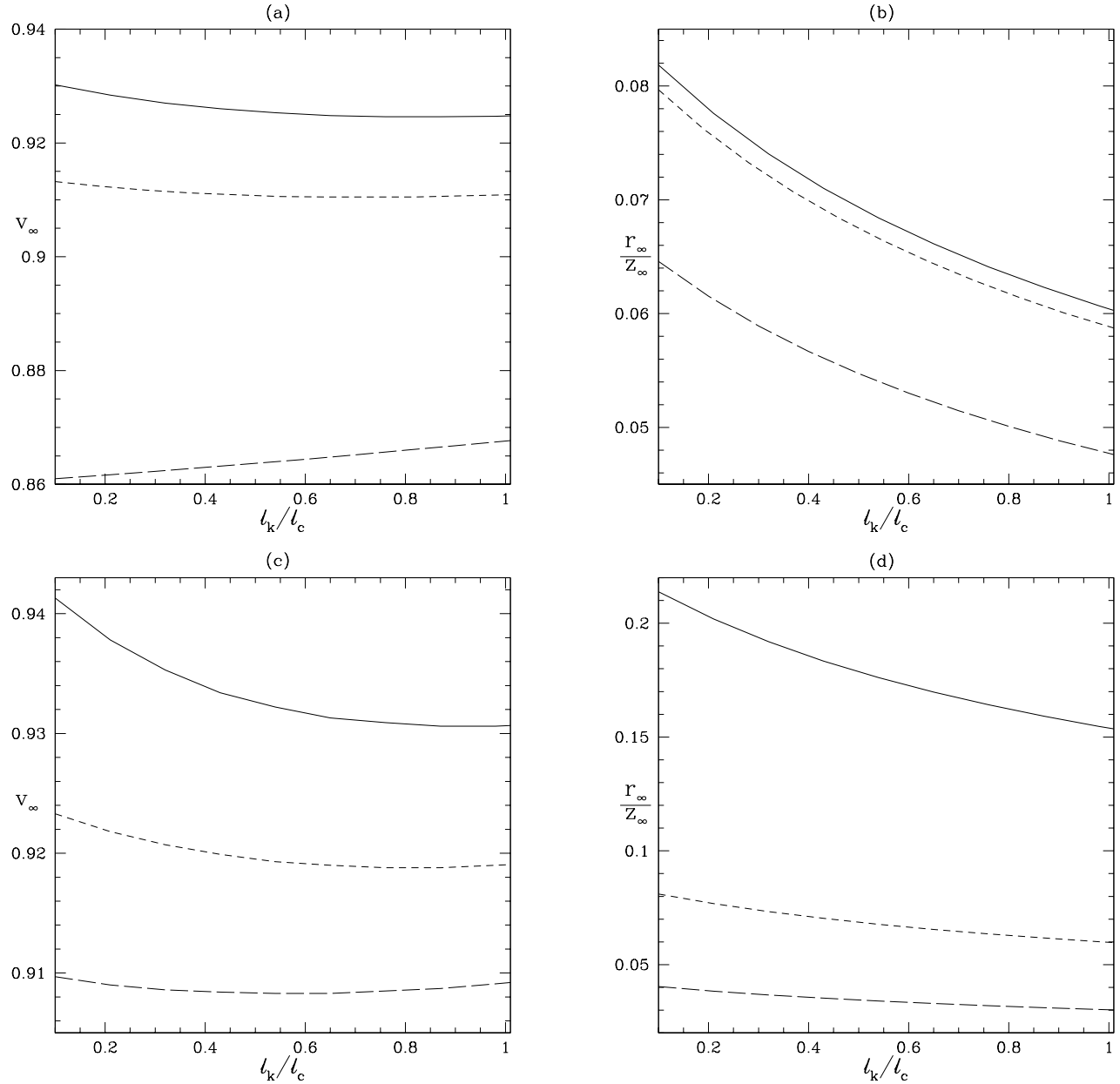


Figure 12. Variation of v_∞ (a) and r_∞/z_∞ (b), with ℓ_k/ℓ_c , for $\ell_c = 0.5$ (solid), $\ell_c = 0.3$ (dashed) and $\ell_c = 0.1$ (long-dashed); $x_s = 20r_g$. Variation of v_∞ (c) and r_∞/z_∞ (d), with ℓ_k/ℓ_c , for $x_s = 10r_g$ (solid), $x_s = 20r_g$ (dashed) and $x_s = 30r_g$ (long-dashed); $\ell_c = 0.4$. For all the figures $r_i = 2r_g$.

We have seen in the preceding sub-section that we achieve better collimation with larger shock location. In Fig. (12c), we plot v_∞ with ℓ_k/ℓ_c , for $x_s = 10r_g$ (solid), $x_s = 20r_g$ (dashed) and $x_s = 30r_g$ (long-dashed), where $\ell_c = 0.4$ and $r_i = 2r_g$ are kept fixed. We find for $x_s = 10r_g$ (solid), v_∞ varies from above $0.94c$ to just above $0.93c$, on the other hand for $x_s = 30r_g$ (long-dashed), v_∞ varies slightly and is always a little less than $0.91c$. Interestingly for smaller values of x_s , increasing ℓ_k/ℓ_c , or in other words proportionally increasing the KD radiation has relatively larger effect (although much smaller than equivalent increase in ℓ_c).

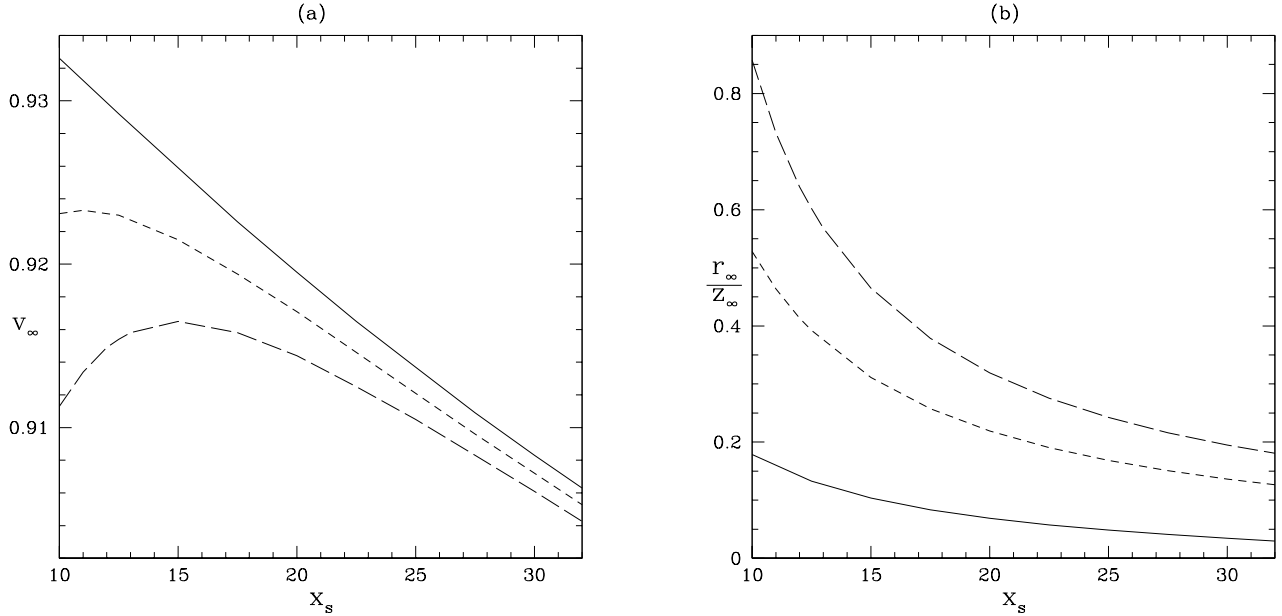


Figure 13. Variation of v_∞ (a) and r_∞/z_∞ (b) with x_s , for $r_i = 2r_g$ (solid), $r_i = 4r_g$ (dashed) and $r_i = 6r_g$ (long-dashed). For both the figures $\ell_c = 0.4$ and $\ell_k = 0.2$.

For larger x_s , the most luminous part of KD ($\sim 4r_g$) is missing so its contribution to the components of radiative moments are quite low, and as a result increasing ℓ_k has a negligible effect on v_∞ . In Fig. (12d), corresponding r_∞/z_∞ is plotted with ℓ_k/ℓ_c , for $x_s = 10r_g$ (solid), $x_s = 20r_g$ (dashed) and $x_s = 30r_g$ (long-dashed), where $\ell_c = 0.4$ and $r_i = 2r_g$ are kept fixed. It is also seen that, decrease of r_∞/z_∞ with increasing ℓ_k/ℓ_c , is more stronger for smaller values of x_s (solid) than the larger values (long-dashed).

Thus we see that, if $\ell_c > 0.2$, $x_s > 20r_g$, $1 > \ell_k/\ell_c < 0.5$, for $r_i \sim 2r_g$, we get relativistic ($v_\infty > 0.9c$) and collimated jets ($r_\infty/z_\infty < 0.1$), which means jets will be better collimated in intermediate hard states.

We already know that higher proportions of KD radiation, higher values of x_s etc are needed for collimation, while ℓ_c accelerates the jets. Still one should not forget about injection radius of the jets, because we have seen that increase in r_i can disturb collimation as well as produce slower jets. We now study the effect of r_i , on jet solution for higher values of ℓ_k/ℓ_c and increasing x_s .

In Fig. (13a), v_∞ is plotted with x_s for $r_i = 2r_g$ (solid), $r_i = 4r_g$ (dashed), $r_i = 6r_g$ (long-dashed), where $\ell_c = 0.4$ and $\ell_k = 0.2$, *i.e.*, $\ell_k/\ell_c = 0.5$. The ratio of CENBOL and KD luminosity is assumed to be around 0.5, in order to aid collimation. We now see a new feature, for lower r_i (solid) v_∞ decreases monotonically with x_s , but for higher r_i (long-dashed) v_∞ at first increases up to $x_s \sim 15r_g$ and then decreases. From Figs. (5a-j), we see

that all the radiative moments peaks around $\sim 2r_g$, just above the inner surface of the CENBOL, and also have very strong gradients as one moves along the CENBOL surface towards x_s . For larger x_s the gradients are smoother, but for smaller x_s gradients becomes stronger. So when $r_i (= 6r_g)$ is larger for small x_s (long-dashed), then, the radiative moments received at r_i is small, because, the presence of strong gradients in all the moments, makes all of them peak around $2r_g$, and sharply decrease at $6r_g$. As x_s increases, for $r_i = 6r_g$, the gradients are becoming smoother, and $r_i = 6r_g$ relatively becomes closer to the axis for larger x_s . So, as x_s increases from $10r_g$ to $15r_g$, the jet material at $r_i = 6r_g$, receives larger values of radiative moments, resulting in increase of v_∞ . Increasing x_s further, decreases v_∞ , because the CENBOL intensity decreases so much that the driving force of radiation decreases anyway.

In Fig. (13b), r_∞/z_∞ is plotted with x_s for $r_i = 2r_g$ (solid), $r_i = 4r_g$ (dashed), $r_i = 6r_g$ (long-dashed), where $\ell_c = 0.4$ and $\ell_k = 0.2$, *i.e.*, $\ell_k/\ell_c = 0.5$. The relative spread decreases monotonically with x_s , as the collimation depends on whether $f^r < 0$ or $f^r > 0$. With increasing x_s , f^r becomes negative (directed towards the axis) in a larger domain, thus helping in collimation. Thus we see that for $x_s > 22r_g$, $r_i < 4r_g$, $\ell_c \sim 0.4$ and $\ell_k/\ell_c \gtrsim 0.5$, we have jets with relativistic terminal speed $\gtrsim 0.9c$ and $r_\infty/z_\infty \lesssim 0.2$, in other words we have collimated and relativistic jets.

5 DISCUSSION AND CONCLUDING REMARKS

In this paper, we have studied the interaction of radiation with pair dominated jets from TCAF disc model. We have ignored the details of the mechanism of production of pair dominated jets. High energy photons can produce particle-antiparticle pairs close to the inner edge of a disk. It is well known, if the photon energy $h\nu \gtrsim 2mc^2$, then an electron-positron pair may be created, where h is the Planck's constant, ν is photon frequency and m is the electron (or positron) mass. If, on the other hand, electron and positron collide it will annihilate each other to produce two Gamma-ray photons, a process called pair annihilation. Evidently, to produce pair dominated jets pair production has to dominate pair annihilation process, as has been theoretically investigated by Mishra & Melia (1993) and Yamasaki *et al.* (1999). Observationally, electron-positron jets were suggested in galactic black hole candidate Nova Muscae 1991/GS 1124-684 (Sunyaev *et al.* 1992), GRS 1915+105 (Mirabel & Rodriguez 1998), in quasar 3C279 (Wardle *et al.* 1998). Though there is little

doubt about the existence of pair dominated jets, radiative acceleration/collimation of such jets on the other hand is a different issue altogether. If the pairs are produced to such an extent that the jet medium is optically thick then the process discussed in this paper fails. For optically thick medium, radiation drag terms are not there, but disc intensity will fall off exponentially. We have not considered such details, because considering such details involves self-consistent treatment of the inflow-outflow solutions around black holes. The present effort confines itself to extend our earlier work (Paper-I) to rotating jets.

The post-shock torus of the TCAF model, produces normal plasma jets and high energy photons. In this paper we have considered the electron positron jets were produced within the funnel like region of the post-shock torus. In contrast to Paper-I, we have computed all the different moments of radiation field for axial and off-axial points. Furthermore, in Paper-I, we did not consider the Doppler shift of radiation due to the disc motion. The rotational motion of matter on the disc surface will generate an azimuthal component of radiative flux. The Doppler effect term also induces non-uniformity in frequency integrated intensity of the CENBOL, while in Paper-I the CENBOL intensity was uniform. This non-uniformity of CENBOL intensity resulted in strong gradients in the radiative moments around the inner edge of the CENBOL.

The motion of the Keplerian disc is primarily rotation dominated and its expression is known analytically even in general relativity. While the motion of matter in the post-shock torus has no simple analytical expression. Since we were not considering inflow-outflow solutions self-consistently, we needed to make a proper estimate of the motion of post-shock matter. Close to the black hole the infall timescale is much smaller than the viscous time scale so the angular momentum of in-falling matter is almost constant near the black hole. Thus we assumed wedge flow for the motion of in-falling matter along the inner surface of the post shock torus, and solved geodesic equations. The post-shock surface motion may be a little over estimated, as pressure gradient terms are ignored. One could have used Paczyński-Wiita potential, but as this potential blows up at the horizon, the geodesic equations are solved in general relativistic realm. Another reason for estimating the inflow velocities in general relativity is to ensure that the rotational velocities of in-falling matter should tend to become zero as one comes closer to the central object.

The Doppler effect on CENBOL intensity expression [Eq. (8e)], is correct up to first order in \tilde{u}/c . We have chopped off the CENBOL at $x_{in} = 2r_g$, and the velocity field of the

CENBOL is such that at $x_{in} < x < x_s$, $\gamma_{\tilde{u}} \sim 1$. At $x < x_{in}$, $\gamma_{\tilde{u}}$ sharply increases. Thus taking first order correct Doppler term in Eq. (8e) is consistent.

In this paper, we solved for three equations to find three variables v_s , λ and r , for which three injection values corresponding to the three variables were supplied. All the other parameters like x_{in} , x_s , x_o , ℓ_c , \dot{m}_k , and the disc velocity components \tilde{u} and \tilde{u}_K were supplied to compute various independent components of radiation stress tensor or, in other words, all the moments of radiation field.

It has been noticed, that the radiation from Keplerian disc has marginal influence in determining v_s and λ , while has a greater role in determining r . As has been explained above, collimation depends partly on reducing angular momentum of the jet as well as pushing it towards the axis by the radial component of radiative flux. Within the funnel like region radiative flux from the Keplerian disc is negative because of the geometry of the TCAF model. Furthermore, the azimuthal component of the flux from it is also weak compared to the other components, hence the angular momentum gained by Keplerian radiation is small. In contrast, the radial flux from the CENBOL is weakest amongst all the other components, although, because of the special directiveness of the CENBOL, the radial flux is also towards the axis, close to the black hole. However, because of the small size of the CENBOL, at $z \sim 100r_g$, it approaches a point source and hence the radial flux is positive and spreads the jet. But drag terms along r and also the fact that radial flux from CENBOL is weakest amongst its all other components, makes the spreading small. The situation dramatically changes if the injection radius is increased. As r_i is increased, the radial flux increases and is directed more and more away from the axis. On the top of that, the drag terms along ϕ becomes weaker hence reduction of angular momentum decreases. The net effect is, the jet spreads. On the top of that, with increasing r_i , the CENBOL intensity goes down so the force driving the jets are less, resulting in slower jets. On the other hand, collimation is better with increasing x_s . Increasing x_s , makes the radial flux from CENBOL become directed towards the axis in a greater part of the funnel like region, which pushes the jet and helps in collimation, although as x_s is increased the radiation from Keplerian disc has lesser influence in determining r .

In the present paper we have restricted our analysis to non-rotating black holes only. It will be interesting to extend this study, to a Kerr black hole, because the higher efficiency around a Kerr black hole will produce more intense radiation field, and may produce terminal speeds higher than what we have observed in this paper. As the spectrum from TCAF disc

around a Kerr black hole is yet to be computed, so the issue of finding the spatial dependence of the disc intensity for a Kerr black hole is an open problem as yet.

We conclude that, if radiative process is the main accelerating and collimating process then,

(i) Electron-positron jets are accelerated to highly relativistic terminal speed, as well as, is collimated by the radiations from two component accretion disc model.

(ii) The space dependent part of the radiative moments from the post-shock region, dominates the corresponding moments from the Keplerian disc.

(iii) The CENBOL radiation is the main accelerating agent, but the Keplerian disc radiation has marginal influence in acceleration.

(iv) The drag terms in the azimuthal direction is greater than the radiative flux term in the same direction, hence the radiation removes angular momentum from the jet, near the jet base.

(v) Collimation is partly brought about by removal of angular momentum, and partly by the inward direction of the radial flux.

(vi) As the radial flux of the Keplerian disc is towards the axis, Keplerian radiation helps in collimation.

(vii) Collimation is better achieved for larger values of shock location and lower values of injection radius.

(viii) As CENBOL radiation is the main accelerating agent and Keplerian disc radiation is a good collimator, we conclude that, if this is the main process for acceleration and collimation then, highly relativistic and collimated jets should be observed in intermediate hard states ($\ell_k/\ell_c \lesssim 1$), and not in extreme hard states ($\ell_k/\ell_c \ll 1$).

(ix) Drawing concrete conclusion, our study shows, if shock in accretion is between $20r_g - 30r_g$, injection radius $r_i < 4r_g$, CENBOL luminosity $\ell_c \gtrsim 0.2L_{\text{Edd}}$ and $\ell_k/\ell_c \sim 0.5$, then the jets will have terminal speed greater than 90% the velocity of light, and the terminal relative spread will be less than 20%.

ACKNOWLEDGEMENTS

The author acknowledges a grant from ESA Prodex project, ESA contract No. 14815/00/NL/SFe. The author also thanks Professor Sandip K. Chakrabarti of the S. N. Bose National Centre for Basic Sciences (India), for making valuable suggestions in preparing the manuscript.

REFERENCES

- Biretta, J. A., 1993, in *Astrophysical Jets*, Burgerella, D., Livio, M., O’Dea, C., eds, Volume 6 Space Telescope Science Symposium series, Cambridge University Press, Cambridge, p. 263
- Chakrabarti, S. K. 1989, *ApJ* 347, 365 (C89)
- Chakrabarti, S. K., 1990, *MNRAS* 243, 610 (C90)
- Chakrabarti, S. K., Titarchuk, L., 1995, *ApJ* 455, 623 (CT95)
- Chakrabarti, S. K., 1996, *ApJ* 464, 664 (C96)
- Chakrabarti, S. K., Titarchuk, L., Kazanus, L., Ebisawa, K., 1996 *A & AS* 120, 163 (CTKE96)
- Chakrabarti, S. K., 1997, *ApJ* 484, 313 (C97)
- Chakrabarti, S. K., 1998, in Chakrabarti, S. K., ed., *Proc. Observational Evidence For Black Holes In The Universe*. Kluwer Academic Publishers, Dordrecht, p. 19
- Chakrabarti, S. K., 1999, *A&A* 351, 185
- Chattopadhyay, I., Chakrabarti, S. K., 2000, *Int. Journ. Mod. Phys. D* 9, 717
- Chattopadhyay, I., Chakrabarti, S. K., 2002a, *MNRAS* 333, 454
- Chattopadhyay, I., Chakrabarti, S. K., 2002b, in Durouchoux, P., Fuchs, Y., Rodriguez, J., eds, *Proc. of the 4th Microquasar Workshop*, CSP, Kolkata, p. 118
- Chattopadhyay, I., Das, S., Mandal, S., Chakrabarti, S. K., 2003, in Chakrabarti, S. K., Das, S., Basu, B., Khan, M., eds, *Proc. Recent Trends in Astro and Plasma Physics in India*, CSP, Kolkata, p. 76
- Chattopadhyay, I., Das, S., Chakrabarti, S. K., 2004, *MNRAS* 348, 846 (Paper-I)
- Das, T. K., Chakrabarti, S. K., 1999, *Class. Quant. Grav.* 16, 3879
- Das, S., Chattopadhyay, I., Nandi, A., Chakrabarti, S. K., 2001, *A&A* 379, 683
- Ebisawa, K., Titarchuk, L., Chakrabarti, S. K., 1996, *PASJ* 48, 59
- Fukue, J., 1987, *PASJ* 39, 309
- Fukue, J., 1996, *PASJ* 48, 631
- Fukue, J., Tojyo, M., Hirai, Y., 2001, *PASJ* 53 555
- Gallo, E., Fender, R. P., Pooley, G. G., 2003, *MNRAS*, 344, 60
- Hirai, Y., Fukue, J., 2001, *PASJ*, 53, 285
- Icke, V., 1980, *AJ* 85(3), 329
- Icke, V., 1989, *A&A* 216, 294

- Junor, W., Biretta, J. A., Livio, M., 1999, *Nature*, 401, 891
- Liang, E. P. T., Thompson, K. A., 1980, *ApJ* 240, 271L
- Mihalas, D., Mihalas, B. W., 1984, *Foundations of Radiation Hydrodynamics*, Oxford University Press, Oxford
- Mirabel, I. F., Rodriguez, L. F., 1994, *Nat* 371, 46
- Mirabel, I. F., Rodriguez, L. F., 1998, *Nat* 392, 673
- Mishra, R., Melia, F., 1993, *ApJ*, 419 L25
- Novikov, I. D., Thorne, K. S., 1973, in *Black Holes*, C. Dewitt and B. Dewitt (eds.), Gordon and Breach, New York, p. 343 (NT73)
- Orihara, S., Fukue, J., 2003, *PASJ* 55, 953
- Paczynski, B., Wiita, P., 1980, *A&A* 88, 23
- Piran, T., 1982, *ApJ* 257, L23
- Shakura, N. I., Sunyaev, R. A., 1973, *A&A* 24, 337
- Smith, D. M., Heindl, W. A., Markwardt, C. B., Swank, J. H., 2001, *ApJ* 554, L41
- Smith, D. M., Heindl, W. A., Swank, J. H., 2002, *ApJ* 569, 362
- Sunyaev, R., Churazov, E., Gilfanov, M., Dyachkov, A., Khavenson, N., Grebenev, S., Kremnev, R., Sukhanov, K., 1992, *ApJ*, 389, L75
- Tajima, Y. and Fukue, J. 1996, *PASJ*, 48, 529
- Tajima Y. and Fukue J. 1998, *PASJ* 50, 483
- Yamasaki, T., Takahara, F., Kusunose, M., 1999, *ApJ*, 523, L21
- Wardle, J. F. C., Homan, D. C., Ojha, R., Roberts, D. H., 1998, *Nat* 395, 457
- Watarai K. and Fukue J. 1999, *PASJ* 51, 725
- Zensus, J. A., Cohen, M. H., Unwin S. C., 1995, *ApJ* 443, 35

APPENDIX A: ESTIMATION OF POST-SHOCK INFLOW VELOCITY

The CENBOL is assumed conical, *i.e.*, motion of post-shock flow is assumed wedge flow. Let us solve the geodesic equation along the radial coordinate \bar{r} , such that $\bar{r}^2 = x^2 + y^2$ where x & y defines cylindrical radial and axial coordinated of CENBOL inner surface. The geodesic equation for conical inflow around a non-rotating black-hole is;

$$\tilde{u}^\nu \frac{\partial \tilde{u}^{\bar{r}}}{\partial x^\nu} + \Gamma_{\mu\nu}^{\bar{r}} \tilde{u}^\mu \tilde{u}^\nu = 0. \quad (\text{A1})$$

The radial velocity & azimuthal velocity is defined as

$$\tilde{u}_{st}^2 = -\frac{\tilde{u}_{\bar{r}}\tilde{u}^{\bar{r}}}{\tilde{u}^0\tilde{u}_0} \quad \text{and} \quad \tilde{u}_{\phi}^2 = \frac{(\bar{r}-1)\lambda_{in}^2}{\bar{r}^3} \quad (\text{A2})$$

Defining $\tilde{u} = \tilde{u}_{st}/(1 - \tilde{u}_{\phi}^2)^{1/2}$, reduces Eq. (A.1) to;

$$\frac{d\tilde{u}}{d\bar{r}} = -\frac{1/2 + (\tilde{u}^2/2 - \bar{r} + 1)\tilde{u}_{\phi}^2}{\bar{r}(\bar{r}-1)\gamma_{\tilde{u}}\tilde{u}}, \quad (\text{A3})$$

where, $\gamma_{\tilde{u}}^2 = 1/(1 - \tilde{u}^2)$.

Equation (A.3) is solved by supplying the value of $\tilde{u}_{stin} = -0.01$ at $\bar{r}_{in} = \sqrt{x_s^2 + h_s^2}$. As \tilde{u}_{st} is the 3-velocity of inflow, so $\tilde{u}_{st} < 0$, i.e., at $\bar{r} = 1r_g$, $\tilde{u}_{st} = -1$, $\tilde{u}_{\phi} = 0$.